TAMPEREEN TEKNILLINEN YLIOPISTO
TAMPERE UNIVERSITY OF TECHNOLOGY

Harri Ali-Löytty

Microalloying Mediated Segregation and Interfacial Oxidation of FeCr Alloys for Solid-Oxide Fuel Cell Applications

Tampere 2013

Harri Ali-Löytty

Microalloying Mediated Segregation and Interfacial Oxidation of FeCr Alloys for Solid-Oxide Fuel Cell Applications

Thesis for the degree of Doctor of Science in Technology to be presented with due permission for public examination and criticism in Konetalo Building, Auditorium K1702, at Tampere University of Technology, on the 19th of February 2013, at 12 noon.

Doctoral candidate: Harri Ali-Löytty, M.Sc.
Surface Science Laboratory
Optoelectronics Research Centre
Tampere University of Technology

Supervisor: Mika Valden, prof.
Surface Science Laboratory
Optoelectronics Research Centre
Tampere University of Technology

Pre-examiners: N. Stewart McIntyre, emeritus prof.
Department of Chemistry
University of Western Ontario

Philippe Marcus, prof.
Laboratoire de Physico-Chimie des Surface
École Nationale Supérieure de Chimie de Paris

Opponent: Anders Nilsson, prof.
Center for Interface Science and Catalysis
SLAC National Accelerator Laboratory
Stanford University

ABSTRACT

Ferritic stainless steels (FeCr-based alloys with low Ni content) have gained recent interest due to their excellent corrosion resistance, mechanical strength, and competitive price, which make them an attractive choice for many energy applications, for example, energy conversion and exhaust systems. The corrosion resistance results from the Cr-rich protective oxide layer that forms spontaneously under oxidizing conditions. At elevated temperatures, oxidation resistance can be enhanced by controlled surface treatments or by microalloying with elements that affect the oxide layer formation through segregation and interfacial oxidation. Today, further alloy development is required concerning the high-temperature oxidation resistance due to the increased operation temperatures. Furthermore, new alloy materials that form an electrically conductive non-volatile oxide layer under high-temperature conditions are required for the solid-oxide fuel cell interconnect applications.

In this thesis, the segregation and oxidation phenomena on non-stabilized and Ti–Nb stabilized ferritic stainless steel alloys were investigated at 50–800 °C by photoemission spectroscopy, inelastic electron energy-loss background analysis, and electrochemical impedance spectroscopy. Firstly, the influence of controlled surface treatments on the initial stages of oxidation was investigated. The surface enrichment of Cr was induced by H_2O preadsorption at low temperatures and by thermally induced cosegregation with N at high temperatures. The Cr-enriched surface was found beneficial against further oxidation by O_2, but the effect was the most pronounced at low temperatures where the thermal diffusion of ions is not fast enough to support the oxidation.

Secondly, microalloying with Nb was shown to improve the electrical properties of ferritic stainless steel alloys at 650 °C. The role of excess Nb was attributed to its high segregation rate and formation of conductive oxides at the oxide–metal interface. Furthermore, the Nb alloying induced the formation of (FeNbSi)-type Laves intermetallic phase in the alloy, which resulted in the non-uniform distribution of electrically resistive SiO_2 at the interface. Therefore, the results presented in this thesis can be applied to design ferritic stainless steel alloys and surface treatments that facilitate the formation of the protective oxide layer with the optimum composition under various demanding application conditions, particularly, in the solid-oxide fuel cells.

ACKNOWLEDGEMENTS

CONTENTS

LIST OF PUBLICATIONS

This thesis consists of the following publications:

I. P. Jussila, **H. Ali-Löytty**, K. Lahtonen, M. Hirsimäki, and M. Valden, *Inhibition of initial surface oxidation by strongly bound hydroxyl species and Cr segregation: H_2O and O_2 adsorption on Fe–17Cr*, Surface Science **603** (2009) 3005–3010.

II. **H. Ali-Löytty**, P. Jussila, M. Hirsimäki, and M. Valden, *Influence of CrN surface compound on the initial stages of high temperature oxidation of ferritic stainless steel*, Applied Surface Science **257** (2011) 7783–7791.

III. **H. Ali-Löytty**, P. Jussila, T. Juuti, L.P. Karjalainen, A.A. Zakharov, and M. Valden, *Influence of precipitation on initial high-temperature oxidation of Ti–Nb stabilized ferritic stainless steel SOFC interconnect alloy*, International Journal of Hydrogen Energy **37** (2012) 14528–14535.

IV. **H. Ali-Löytty**, P. Jussila, and M. Valden, *Optimization of the electrical properties of Ti–Nb stabilized ferritic stainless steel SOFC interconnect alloy upon high-temperature oxidation: the role of excess Nb on the interfacial oxidation at the oxide–metal interface*, International Journal of Hydrogen Energy **38** (2013) 1039–1051.

AUTHOR'S CONTRIBUTION TO THE PUBLICATIONS

The author had the main responsibility for the planning and organizing of the experiments for Papers II–IV. For all the Papers, the author was largely responsible for the carrying out the significant part of the PES experiments and all the EIS experiments. Furthermore, the author performed the data-analysis and wrote the original manuscripts for Papers II–IV, and contributed to the preparation of the original manuscript for Paper I.

ABBREVIATIONS AND SYMBOLS

2D, 3D	Two-dimensional, three-dimensional
a	Activity
AC	Alternating current
AISI	American Iron and Steel Institute (designation of steel grades)
AOD	Argon-Oxygen-Decarburization
APPES	Ambient pressure photoelectron spectroscopy
ARXPS	Angle resolved X-ray photoelectron spectroscopy
bcc	Body-centered cubic crystal structure
bct	Body-centered tetragonal crystal structure
c	Relative concentration of an element
C	Capacitance
CCD	Charge-coupled device
CLS	Core level shift
CPE	Constant phase element
d	Layer thickness
DC	Direct current
E_0	Initial kinetic energy of an electron
E_B	Electron binding energy
E_K	Electron kinetic energy
$E_{vac,s}$	Energy level of vacuum
EDS	Energy-dispersive X-ray spectroscopy
EIS	Electrochemical impedance spectroscopy
EN	European Standard (designation of steel grades)
eV	Electron volt (the unit of energy), $1 \text{ eV} = 1.6 \times 10^{-19} \text{ J}$
f	Absolute concentration of atoms, AC signal frequency
F	Primary excitation spectrum
FAT	Fixed analyzer transmission
fcc	Face-centered cubic crystal structure
FESEM	Field emission scanning electron microscope
FRA	Frequency response analyzer
G	Electron energy distribution function
G^0	Standard Gibbs free energy
HIKE	High kinetic energy photoelectron spectroscopy

I	PES peak intensity
IMFP	Inelastic mean free path of an electron
J	PES spectrum
L	Langmuir (the unit of gas exposure), 1 L = 1.3×10^{-6} mbar s
MCP	Micro-channel plate
P	Pressure
PEEM	Photoemission electron microscopy
PES	Photoemission spectroscopy
μPES	Micro-photoemission spectroscopy
PVD	Physical vapor deposition
R	Resistance
R	Molar gas constant (8.314 472 J mol^{-1} K^{-1})
S	Atomic sensitivity factor
SCLS	Surface core level shift
SOFC	Solid-oxide fuel cell
SPELEEM	Spectroscopic photoemission and low-energy electron microscope
SPEM	Scanning photoelectron microscope
T	Transmission function of an electron energy analyzer, temperature
t_{OX}	Oxide layer thickness
UHV	Ultra high vacuum
XAS	X-ray absorption spectroscopy
XPEEM	X-ray photoemission electron microscopy
XPS	X-ray photoelectron spectroscopy
z	Excitation depth
Z'	Real part of the impedance
Z''	Imaginary part of the impedance
$h\nu$	Photon energy
θ	Emission angle of electrons
λ	Inelastic mean free path of an electron
σ	Photoionization cross-section
τ	Time constant
ϕ_{sp}	Spectrometer work function
ϕ_s	Surface work function
Ω	Solid angle

1 INTRODUCTION

A century has elapsed since stainless steels (FeCr-based alloys) were first invented and produced in 1912 [1]. Today, these alloys are widely utilized in application areas from everyday domestic appliances to construction and process industry, where excellent corrosion properties combined with high mechanical strength are demanded for the structural materials. Particularly, the stainless steels are optimized material choices for energy applications (e.g., energy conversion and exhaust systems) that operate under high-temperature corrosive environments where the materials performance and lifetime are critical issues. Therefore, the increased use of the corrosion-resistant stainless steel materials, where appropriate, is in a key role to decrease the cost of corrosion, which has been estimated to be > 3% of the nation's gross domestic product in the industrialized countries [2].

Ferritic stainless steels with low Ni content have gained recent interest as cost-effective alternatives for traditional austenitic grades (FeCrNi-based alloys) due to the volatile Ni price. In addition, ferritic grades obtain excellent thermal properties and oxidation resistance, which make them readily suitable for many high-temperature energy applications. However, due to the global demand for higher energy efficiency and cleaner environment, the operation temperatures of energy conversion and exhaust systems are increasing, which means more and more challenging requirements for the material resistance, particularly, against high-temperature oxidation. Furthermore, new energy sources (e.g., fuel cells) have set new material requirements that have been traditionally unheeded in the alloy development. For example, the solid-oxide fuel cell interconnect alloy must remain electrically conductive and have low volatility under the operation conditions, which are both current challenges for the common ferritic stainless steel grades.

The excellent corrosion resistance stems from the formation of a protective oxide layer under suitable conditions. This Cr-rich oxide layer grows only 2–3 nm thick at room temperature, and furthermore it is self-healing if damaged. At elevated temperatures, the oxide layer grows thicker and remains protective if the alloy composition is adjusted to withstand such conditions [3]. Therefore, the enhanced corrosion resistance of novel stainless steel grades can be achieved by microalloying with elements that affect the formation of the oxide layer. Besides the corrosion properties, the above-mentioned challenges that are related to the oxide

layer properties, can be addressed and overcome by intelligent microalloying. Alternatively, surface properties can be improved by controlled surface treatments and coatings.

The development of the oxide layer properties requires the investigation of the surface segregation and oxidation phenomena starting from the initial stages, i.e., from the adsorption of O_2 on a metallic surface. The direct observation of such phenomena is possible with surface-sensitive analysis techniques under well-controlled ultra high vacuum (UHV) conditions. The information depth of the surface science methods is limited to the top atomic layers. Therefore, these methods allow for the investigation of the initial stages of different surface processes, the identification of the process-determining steps, and finally, the controlled development of the processes. This methodology is called the surface science approach, and it was the basis for this work.

Photoemission spectroscopy (PES) allows the analysis of different chemical states of elements at the surface and, therefore, it was chosen as the primary analysis technique in this work [Papers I–IV]. In addition, electrochemical impedance spectroscopy (EIS) was utilized to measure electrical properties of the oxide layers [Paper IV]. The experimental work was carried out in Surface Science Laboratory at Tampere University of Technology and at the soft X-ray beamline I311 in the synchrotron radiation facility MAX IV Laboratory (Lund University, Sweden). The studied polycrystalline stainless steel alloys and their bulk chemical analysis were supplied by Outokumpu Stainless Oy (Tornio, Finland).

This thesis is organized as follows: Chapter 2 introduces the stainless steel materials in general, their manufacturing, and development. In addition, it covers the theory behind the studied surface phenomena and their technological relevance in the high-temperature energy applications of ferritic stainless steels, focusing on the solid-oxide fuel cells (SOFCs). Chapter 3 presents the stainless steel alloys studied, the applied experimental procedures, and the surface analytical methods. The emphasis in Chapter 3 is in the versatile exploitation of the PES method. Chapter 4 summarizes the main results of this work related to the optimization of the oxidation properties of ferritic stainless steel alloys by controlled surface modification and microalloying. Finally, Chapter 5 consists of a summary of the results and an outlook for future work.

2 FUNCTIONAL SURFACE PROCESSES ON FeCr ALLOYS

This chapter introduces the stainless steel materials and the theory behind the surface phenomena studied. The focus is on the ferritic stainless steel alloys and their surface properties. Therefore, relevant surface processes to this work, surface segregation and oxidation at the temperature range of 50–800 °C, are emphasized. Accordingly, mechanical properties and other forms of corrosion will not be considered. Finally, the requirements for optimal surface properties of ferritic stainless steels in SOFC applications are discussed.

2.1 Manufacturing and development of ferritic stainless steel alloys

Stainless steels are Fe-based alloys with a minimum of 10.5 m.% Cr. There are three different main types of microstructures that exist in stainless steels: ferritic (body-centered cubic, bcc), austenitic (face-centered cubic, fcc), and martensitic (body-centered tetragonal, bct) [4]. The different microstructures can be obtained by adjusting the steel's chemical composition and manufacturing heat treatments [5]. From these microstructures, stainless steels can be further divided into different classes, which are ferritic (low Ni content), austenitic (typically > 8 m.% Ni), duplex (austeno–ferritic), and precipitation–hardening stainless steels. The mechanical properties of the alloys within each class differ only slightly, whereas the corrosion properties are substantially affected by the exact alloy composition and applied surface treatments. Therefore, application specific enhanced properties can be achieved by careful microalloying (typically < 1 m.%) with various elements. The development of new stainless steel alloys has led to a vast number of different stainless steel grades that exist today. Fig. 2.1 depicts selected ferritic stainless steel grades designated according to the common standards in the order of increasing corrosion resistance.
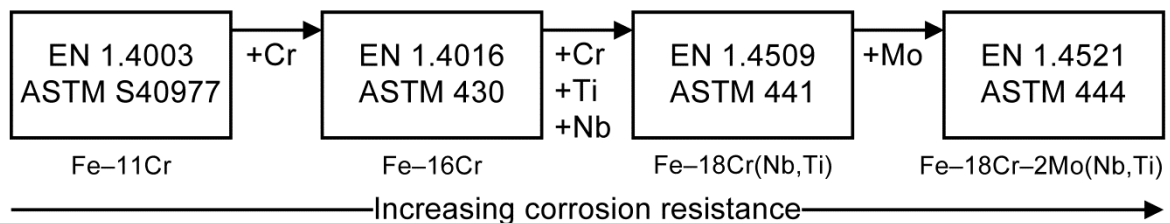
Fig. 2.1 – Selected ferritic stainless steel grades (m.%) in the order of increasing corrosion resistance. In this work EN 1.4016 (Papers I and II) and EN 1.4509 (Papers III and IV) alloys were studied.

In industry, the primary criteria for material selection are cost optimization and life cycle cost reduction. In practice, a higher degree of alloying enhances the properties of the stainless steel but increases the material cost as well. For many applications, the purpose is not to maximize but to optimize the service life of the materials with the expected service life of the application. The cost optimization is a strong reason for why ferritic stainless steel grades have recently replaced the more expensive austenitic grades in applications where material requirements have allowed the use of ferritic grades. Particularly, corrosion resistance of ferritic grades is comparable to that of austenitic grades with similar Cr content [6]. However, some differences in physical properties exist between ferritic and austenitic stainless steels: ferritic grades are magnetizable, obtain higher thermal conductivity and lower coefficient of thermal expansion than non-magnetizable austenitic grades [4].

The manufacturing process of stainless steel begins with the melting and processing of the raw material, which can be either Fe/Cr ore or recycled stainless steel. An average amount of recycled raw material in stainless steel today is about 60%, which could be even higher since stainless steel is almost completely recyclable [7]. However, the amount of recycled raw material is limited due to the long-term annual growth rate of 5% in stainless steel production and typically long service life of 20–30 years. After beneficiation and melting processes, the stainless steel is cast into, for example, a slab, which is further hot- and cold-rolled into a strip with a desired thickness [8]. Then, the strip is annealed to restore the mechanical properties that have been reduced in the cold working and the surface is pickled in an acid bath to restore the corrosion properties. Finally, the strip is rolled into a coil (Fig. 2.2(a)), which can be further processed by the customer.

Fig. 2.2 – (a) A stainless steel coil, (b) a typical grain structure of polycrystalline stainless steel and (c) a hard sphere representation of a ferritic (bcc, body-centered cubic) crystal structure showing typical interstitial sites. The photo (a) by courtesy of Outokumpu Stainless Oy.

Fig. 2.2(b) illustrates the typical grain structure of ferritic stainless steel where ferrite (α) is the primary phase but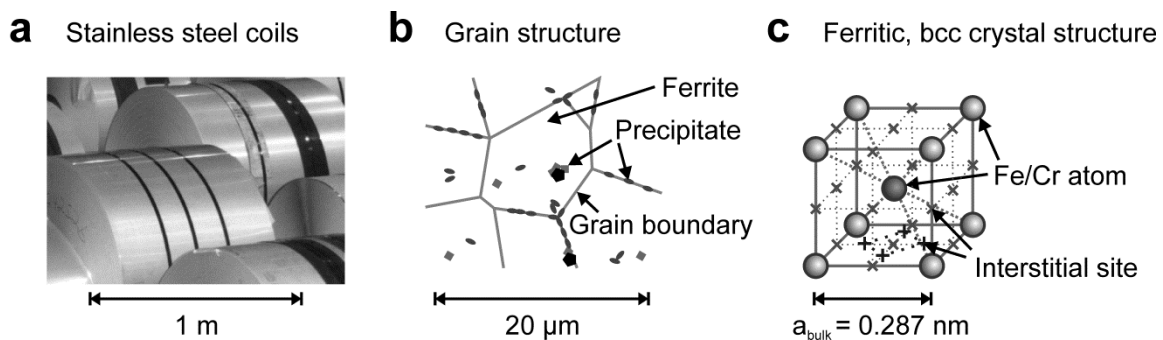 some precipitated second phase particles exist at grain boundaries and grain interiors as well. The mechanical properties of stainless steel are determined by the size and distribution of different phases, which can be greatly influenced by the manufacturing processing parameters. Furthermore, under high-temperature service conditions new phases may precipitate in the ferritic stainless steel, which often deteriorates the mechanical and corrosion properties. Such phases include carbides, nitrides, Cr-rich alpha prime (α′) phase in the temperature range of 370–540 °C, and intermetallic phases (e.g., sigma, chi and Laves) at temperatures 595–1000 °C [9].

The excellent corrosion resistance of stainless steels is largely attributed to the inherent formation of protective Cr-rich oxide layer on the alloy surface under oxidative conditions. A high Cr content in the alloy solution is required to suppress the oxide layer growth and to maintain the high corrosion resistance. However, the precipitation of Cr-rich phases removes Cr from the solution, which decreases the corrosion resistance. The influence of the precipitation on local corrosion may be particularly crucial. The formation of Cr carbides or nitrides at grain boundaries, i.e. sensitization, is detrimental to both mechanical and corrosion properties. The area adjacent to the Cr precipitates is depleted in Cr and, therefore, susceptible to corrosion. This phenomenon is more pronounced in ferritic grades than in austenitic grades, since the diffusion rates of C and N through the interstitial sites in the bcc lattice, depicted in Fig. 2.2(c), are higher than the ones in the fcc lattice [8]. Therefore, the sensitization can be largely avoided by the use of low-carbon content (< 0.03 m.%) ferritic stainless steel or by the use of Ti and/or Nb as stabilizing agents that form more stable carbide and nitride compounds than Cr. The manufacturing of the low-carbon content ferritic stainless steels at a reasonable cost has become possible due to the use of Argon-Oxygen-Decarburization (AOD) method in melting process [10]. In the AOD processing, Ar and O_2 gases are blown into the alloy melt, which affects the decarburization thermodynamics enhancing the burning of the residual carbon from the melt [11].

On the other hand, if the Ti or Nb content in the stainless steel alloy exceeds the required amount to bind all the C and N from the solution, the formation of intermetallic Laves phases Fe_2Ti and Fe_2Nb can take place at elevated temperatures [8]. In addition to Ti and Nb, also Mo has a propensity for Laves phase formation. Traditionally, Mo is added to stainless steels to improve wet corrosion properties, particularly, in chloride environments. Recently, the

formation of these Laves phases has received considerable interest due to their capability to bind Si from the alloy solution, which has been shown to improve electrical properties of the alloy [12]. Conventionally manufactured stainless steel alloys contain some residual amounts of Si and Al that are used as deoxidizing agents in the melting process. As well, both elements are known to improve the high-temperature corrosion resistance [13]. The influence of (FeNbSi)-type Laves phase precipitates and excess Nb on the high-temperature oxidation of EN 1.4509 alloy was studied in Papers III and IV.

In addition to the elemental composition of the alloy, the surface finishing has a strong influence on the corrosion resistance. For example, after the annealing of stainless steel under oxidizing atmosphere in manufacturing processes (i.e., black annealing), the surface is covered with a non-protective thick FeCr oxide layer and a Cr depleted layer beneath it. Therefore, the alloy is subsequently pickled in an acid bath that dissolves the non-protective surface layers and restores the protective Cr-rich oxide layer [14]. Alternatively, annealing can be conducted under reducing H_2 atmosphere (i.e., bright annealing) followed by controlled oxidation at low temperatures, which yields the protective oxide layer.

2.2 Segregation of alloying elements

The surface composition of an alloy can be significantly different from the bulk composition. This is because atoms on the surface are at higher energy situation than the atoms in the bulk, and therefore, the surface must relax to reach the thermodynamically favored minimum energy state. The relaxation may occur by the enrichment of alloying elements with lower surface energy on the surface [15]. This process is called segregation, and it has a significant role on surface and interface processes, such as growth and adhesion of oxides in stainless steels since most alloying elements tend to enrich on surfaces under favorable conditions [16]. The segregation phenomena are particularly crucial in high-temperature processes where diffusion rates of dissolved elements are enhanced. Furthermore, due to the increased extent of the use of recycled material in stainless steel production, it has become more and more important to have control over the segregation of trace or impurity elements.

The diffusion of dissolved elements in an alloy precedes segregation. The diffusion of substitutional elements (Fe, Cr, Mn, Nb, Si) can proceed through place exchange and defects in a metal lattice, whereas light elements (C, N, O) diffuse through interstitial sites [13]. In

addition, grain boundaries can act as fast diffusion channels for all elements. Fig. 2.3 illustrates different segregation phenomena that can be detected in stainless steel alloys under dry conditions. Segregation may take place (1.) on the alloy surface as well as (2.) at grain boundaries or (3.) other interfaces such as at an oxide–metal or coating–metal interface. The enrichment of a dissolved element on a surface may be driven by lower surface energy of the element (i.e., equilibrium segregation) or it may occur via synergetic effects with other elements or compounds. In stainless steel alloys, (4.) the cosegregation of Cr with N is observed, leading to the formation of CrN surface compounds [Paper II]. Furthermore, (5.) segregation of an element may be induced by an adsorbate. Particularly, in stainless steel alloys the adsorption of oxygen or water may induce the segregation of an element with higher oxygen affinity than Fe (e.g., Cr, Si) [16]. In this work, H_2O adsorption induced surface segregation of Cr was observed in Paper I. Finally, segregation of an element may precede (6.) the precipitation of three-dimensional compounds, e.g., carbides and nitrides.
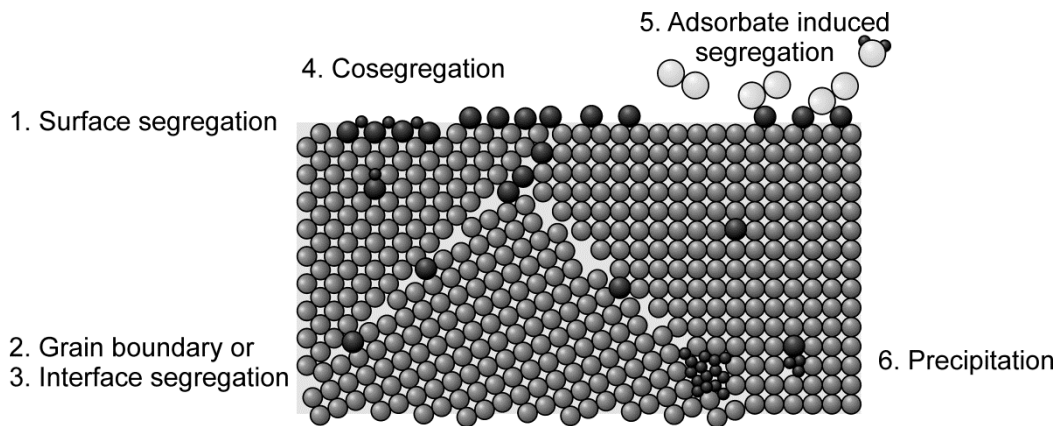
Fig. 2.3 – A schematic illustration of different segregation related phenomena (1.–6.) that may take place in stainless steel alloys. Dark circles represent dissolved elements in FeCr alloy solution (light gray circles). (Adapted from [16].)

The formation of carbide and nitride precipitates as well as the enrichment of minor alloying and trace elements of stainless steel (e.g., P, S, Sn, Sb) at grain boundaries typically cause embrittlement of the alloy [17]. In addition, the segregation of trace elements has implications for the oxidation properties by affecting the adhesion of the oxide layer. For example, the enrichment of S at the oxide–metal interface is known to cause the spallation of the oxide layer [16]. In order to avoid these deleterious consequences, the stainless steel alloy composition must be adjusted at parts-per-million level for some elements. On the other hand, in high-temperature surface treatments under reducing atmosphere (e.g., bright annealing), the segregation of trace elements on the surface may be followed by desirable desorption of trace

element compounds (e.g., H_2S), which reduces the amount of corresponding trace elements in the alloy solution [18]. Furthermore, the particularly important consequence of the segregation phenomena is the formation of protective oxide layer on stainless steel alloys, which can be largely affected by the suitable microalloying with elements that segregate and oxidize at the oxide–metal interface.

Despite the technological importance of the segregation phenomena, the understanding of the related processes, even for simple binary alloy surfaces, is not well developed [19]. For example, the formation of experimentally well-known Cr enriched surfaces on stainless steels should not be favored based on the surface energy consideration because the surface energy of Fe (2.222 J m^{-2}) is lower than that of Cr (3.979 J m^{-2}) [20]. However, it was recently shown theoretically that Cr segregation on FeCr alloy surface is, in fact, driven by magnetic effects [21]. When complex competing magneto-chemical interactions between ferromagnetic Fe and antiferromagnetic Cr were taken into account, it was shown that Cr-containing surface became favorable when the bulk concentration of Cr exceeded 10 at.% [22]. Furthermore, under oxidizing conditions Cr enriched surface forms since the formation of Cr_2O_3 is thermodynamically favored over the formation of Fe oxides (see Section 2.3), and therefore, the adsorption of oxygen is expected to enhance the surface segregation of Cr. In the case of multi-element alloys, the prediction of the surface composition is particularly difficult and only little studied theoretically [23]. Therefore, experimental studies of surface segregation are required for the identification of the critical alloying or trace elements that determine surface processes of microalloyed stainless steels at high temperatures.
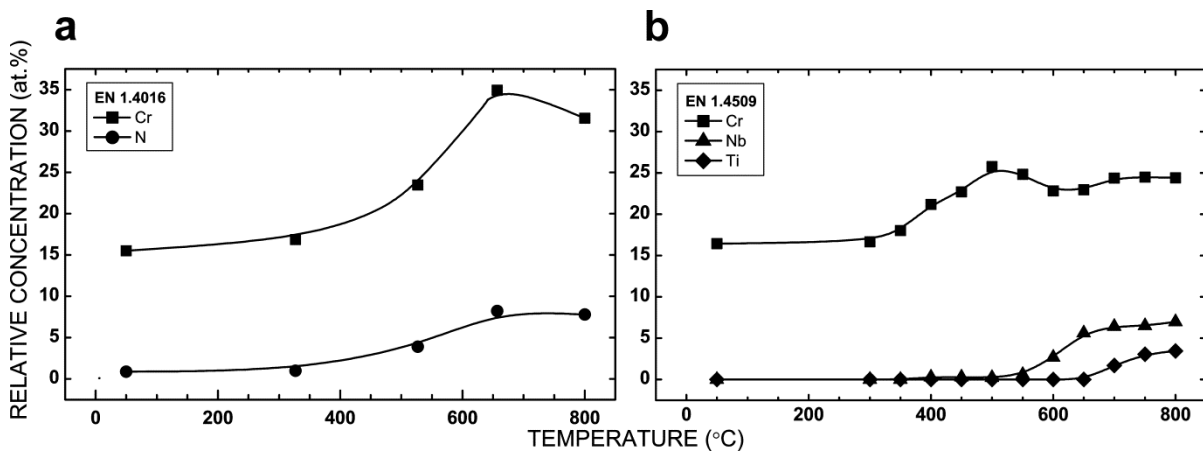

Fig. 2.4 – Relative surface concentration of Cr, N, Nb and Ti (balance Fe) on (a) non-stabilized EN 1.4016 (Fe–17Cr) and (b) Ti–Nb stabilized EN 1.4509 (Fe–19Cr–(Ti,Nb)) after annealing the sputter-cleaned surface for 5 min at different temperatures in UHV environment. (unpublished results)

Fig 2.4 shows an example of a surface segregation experiment on two different stainless steel alloys: (a) a non-stabilized Fe–17Cr (at.%) alloy (EN 1.4016) and (b) a Ti–Nb stabilized Fe–19Cr–(Ti,Nb) (EN 1.4509). The experiments were conducted under UHV conditions by annealing the sputter-cleaned sample at selected temperatures for 5 min. The surface composition (within the information depth of ~ 5 nm) was subsequently analyzed by PES. Initially, below 350 °C the surface composition corresponded closely to the bulk composition on both samples. At higher temperatures, the surface segregation of Cr was detected. However, Cr enrichment on the Fe–17Cr alloy was significantly stronger reaching the value of 35 at.% at 657 °C, whereas the maximum surface concentration of Cr on the Fe–19Cr–(Ti,Nb) alloy was only 25 at.%. From the concomitant increase in the amounts of Cr and N on the Fe–17Cr surface, it was concluded that the enhanced surface enrichment of Cr was due to the cosegregation of Cr with N [Paper II]. In contrast, no segregation of N was observed on Fe–19Cr–(Ti,Nb) alloy, since the free N in the alloy was bound to the stable Ti nitride compounds [Paper III]. Furthermore, the surface enrichment of Nb and Ti was observed on the Fe–19Cr–(Ti,Nb) at temperatures above 550 °C and 650 °C, respectively. Therefore, it was expected that these microalloying elements, which were originally added to the stainless steel alloy as stabilizing agents, affect the high-temperature properties of this alloy. In this work, excess Nb alloying mediated segregation and oxidation phenomena were studied in Papers III and IV.

2.3   Surface and interface oxidation

The excellent surface properties of stainless steel alloys stem from the formation of a protective oxide layer under oxidizing conditions. This Cr-rich oxide layer grows only 2–3 nm thick at room temperature, and it is often designated as the passive layer. At elevated temperatures, the oxide layer grows thicker and remains protective if the alloy composition is adjusted to withstand such conditions [3]. Otherwise, the oxide layer loses its protectiveness, and corrosion occurs. In this work, surface oxidation by O_2 was studied at temperature range 50–800 °C, focusing on the initial stages of oxidation. Many application conditions contain several other oxidizing species, particularly, aqueous environments. However, oxidation by O_2 is the most important corrosion mechanism at temperatures above 300 °C [3].

The understanding of the oxidation phenomena requires thermodynamic and kinetic considerations. Firstly, the oxidation of a metal M can proceed spontaneously according to the chemical reaction

$$\frac{2x}{y}M + O_2 \rightarrow \frac{2}{y}M_xO_y \tag{2.1}$$

if the standard free energy of formation ΔG^0 for the reaction is negative under the considered conditions. The standard free energy of formation values as a function of temperature T for selected bulk oxides of stainless steel alloying elements are presented in Fig. 2.5. In addition to the depicted oxides, these metals may form multiple stable oxides with different stoichiometry or mixed oxide compounds with other metals. For the reaction (2.1), the equilibrium pressure of O_2 (or oxygen activity) that is required to support the oxidation can be expressed as [24]

$$P(O_2) = e^{\Delta G^0/RT}, \tag{2.2}$$

where R is the molar gas constant (8.314 472 J mol^{-1} K^{-1} [25]).
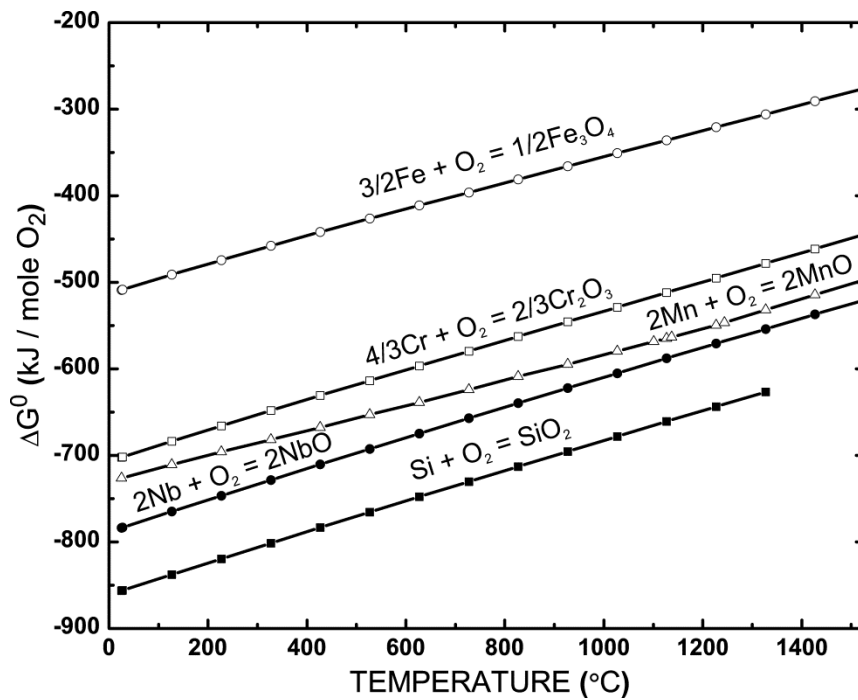
Fig. 2.5 – The standard Gibbs free energy of formation for selected bulk oxides as a function of temperature (Ellingham diagram). Data from: [26,27].

For example at 800 °C, the formation of Fe_3O_4 (−376 kJ /mole of O_2) is not supported under conditions with oxygen partial pressure below 2.7×10^{-17} mbar, whereas more stable SiO_2 (−712 kJ /mole O_2) can form as long as oxygen activity remains above 6.5×10^{-35} mbar. Due to the extremely low equilibrium pressures, all alloying elements of stainless steel form stable oxides under ambient pressure conditions. However, the oxygen activity of the atmosphere in industrial applications, e.g., in combustion chambers, can be significantly different from the ambient air, or the composition of the surrounding atmosphere can be adjusted intentionally. For example, the heat treatment of stainless steel can be conducted under a protective H_2 atmosphere, i.e., under low oxygen activity, which is reductive for all the alloying element oxides.
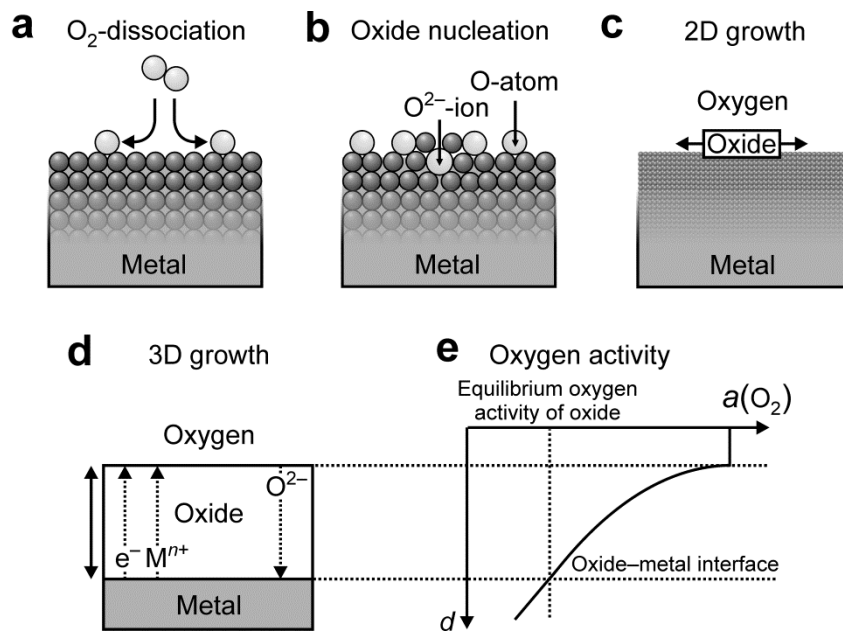
Fig. 2.6 – The initial stages of oxidation and oxide layer growth on a metal surface. Oxidation begins with (a) the dissociative adsorption of an oxygen molecule on the metal surface, which is followed by (b) oxide nucleation, and (c) the 2D growth of the oxide layer. (d) Further oxidation requires the transport of ions and electrons through the oxide layer. (e) Oxygen activity below the oxide layer is lower than the oxygen activity that is required to support the oxidation.

Figs. 2.6(a–d) illustrate the initial stages of oxidation and the oxide layer growth on metal surfaces. The kinetic consideration of the oxidation begins with the interaction between the oxygen in the atmosphere and the metal surface. For FeCr alloys (a) an oxygen molecule is first dissociatively adsorbed on the metal surface [28]. Then, (b) the transition from the adsorption of oxygen to the oxidation of metal requires the penetration of the oxygen atom into the metal and the formation of a chemical bond. This oxide nucleation process has been

proposed to take place via the place exchange process, in which the oxide anion and metal cation interchange positions, and the metal lattice transforms into the oxide compound lattice [29]. Next, (c) the oxide layer grows laterally across the surface forming the first oxide layer. (d) The further growth of the oxide layer requires the diffusion of metal cations and electrons through the oxide layer to the gas–oxide interface, or the diffusion of oxygen anions through the oxide layer to the oxide–metal interface. The growth processes of the oxide layer are essentially different under low- and high-temperature conditions due to the differences in the diffusion processes [29].

Under low temperature conditions, the thermal energy of ions is insufficient to overcome the energy barrier that is required for an ion to diffuse through the oxide layer. Based on the Cabrera–Mott theory, the driving force for the diffusion at low temperatures is the electric field that forms between the oxygen anions on the surface and the metal cations at the oxide–metal interface upon the tunneling of the electrons through the oxide layer [29]. Because the strength of the electric field decreases rapidly with the increasing oxide layer thickness, the growth rate of the oxide layer decreases obeying the logarithmic rate laws of oxidation [29]. This process results in the oxide layer with the thickness in the range of a few nanometers. Therefore, the experimental study of oxidation at the nanoscale requires surface analytical techniques [30,31].

At high temperatures, the thermal diffusion of ions is fast enough to support the oxidation and control the growth rate of the oxide layer, which can be usually described by parabolic kinetics [13]. According to the Wagner theory, the diffusion of ions in an oxide scale proceeds through point defects that are ion vacancies (missing ions) or interstitials (extra ions) [13]. Oxygen anions and metal cations have different types of point defects and, therefore, different diffusion mechanisms that are determined by the oxide structure. Particularly, the presence of grain boundaries in polycrystalline oxides provides fast diffusion paths for ions in comparison to amorphous oxides such as SiO_2. Depending on the proportional diffusion rates of metal cations and oxygen anions, the oxide layer can grow at the surface or at the oxide–metal interface. In the former case, oxidation rate is largely controlled by the composition and pressure of the surrounding atmosphere, whereas in the latter case the properties of the metal affect the rate of oxide growth [29]. Furthermore, from the defective nature of oxides (i.e., deviation from the oxide stoichiometry) follows their semiconductivity. For example, Cr_2O_3 is

a p-type semiconductor because charge is carried by cation vacancies, whereas oxygen deficient Fe_2O_3 (i.e., charge is carried by anion vacancies) is an n-type semiconductor [24].

In a metal alloy, an element that forms the most stable oxide can oxidize preferentially if diffusion of the element is fast enough to support the oxidation, i.e., selective oxidation. Therefore, the formation of more stable Cr oxides is favored over Fe oxides in stainless steel alloys. The Cr_2O_3 oxide layer is referred to as the protective layer, since diffusion processes within the Cr_2O_3 oxide are generally slow and independent of oxygen activity over a wide range, which hinders oxidation further [32]. In stainless steel alloys that form the protective oxide layer, the Cr content is high enough to support the formation of continuous, well adherent Cr_2O_3 layer that grows mainly by the outward diffusion of Cr [13]. However, in many cases the diffusion of Cr in the alloy to the oxide–metal interface is not strong enough to support the Cr_2O_3 layer formation and prevent the formation of non-protective Fe oxides. Accordingly, if the protective oxide layer is damaged under critical conditions, the catastrophic breakaway oxidation can occur with fast linear oxidation kinetic rate [3]. In addition, if the diffusion rate of oxygen in the alloy is stronger than that of Cr (or other element), internal oxidation can occur [13]. Internal oxidation is a pronounced oxidation mechanism at high temperatures, and it is typically detected at grain boundaries where diffusion rates are enhanced.

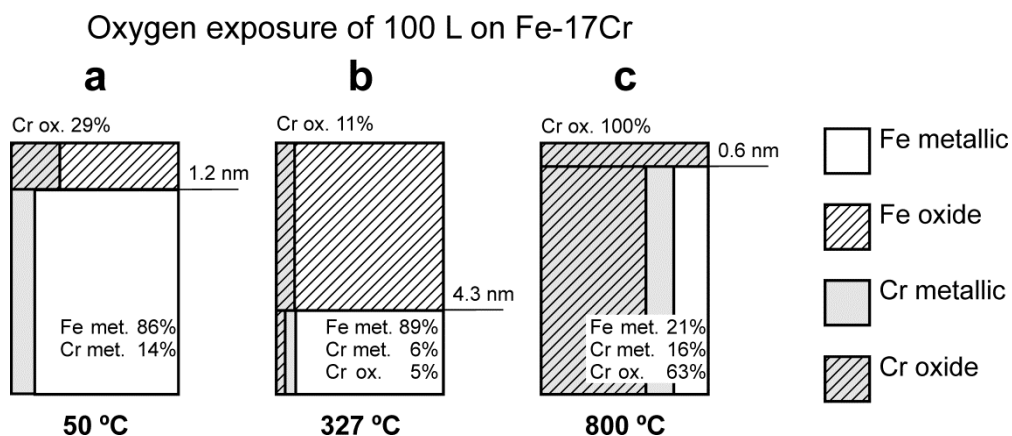Fig. 2.7 – Surface morphology obtained by inelastic electron energy-loss background analysis of Fe–17Cr (EN 1.4016) surface after 100 L oxygen exposure at (a) 50 °C, (b) 327 °C, and (c) 800 °C. Results from Papers I and II.

Fig. 2.7 shows the oxide layer morphology of Fe–17Cr (EN 1.4016) alloy surface after 100 L oxygen exposure at three different temperatures. The figure illustrates the influence of

temperature on the oxide layer composition and the oxidation kinetics. After 100 L oxygen exposure, all oxide layers have transferred from the 2D layer growth to the 3D growth. (a) Only a 1.2 nm thin Cr-rich oxide layer is formed at 50 °C, whereas (b) a 4.3 nm thick Fe-rich oxide layer is formed on the surface at 327 °C. (c) At 800 °C, the surface is covered with a 0.6 nm thick Cr-oxide layer and pronounced internal oxidation of Cr is observed (within the information depth of the analysis ~ 10 nm).

The oxide layer on a stainless steel alloy can consist of several different oxides of different alloying elements. Different oxide compounds in the oxide layer are ordered from the least stable oxides at the surface to the most stable oxides at the oxide–metal interface [13]. This is because the oxygen activity $a(O_2)$ in the oxide layer, depicted in Fig. 2.6(e), decreases with depth, and it is not high enough to support the formation of less stable oxide compounds closer to the oxide–metal interface. Consequently, the formation of the most stable oxides is favored under low oxygen pressure conditions, which was utilized in Papers III and IV to study interfacial oxidation of EN 1.4509 ferritic stainless steel alloy. Particularly, the high-temperature oxidation of stainless steels is affected by the formation of highly stable Si oxides at the oxide–metal interface. The amorphous SiO_2 layer acts as a diffusion barrier to the transport of metal ions to the oxide layer [33]. Therefore, the microalloying of stainless steel with Si enhances high-temperature oxidation resistance.

The oxidation phenomena of stainless steel alloys with various alloying and trace elements are in many cases more complex than described above. For example, since Mn has more stable oxide than Cr (Fig. 2.5), it is expected to form below Cr_2O_3. In contrast, a Mn-rich oxide layer is observed above Cr_2O_3 layer on FeCr alloys that are oxidized at high temperatures [Paper IV]. This is concluded to be due to the rapid diffusion of Mn in Cr_2O_3 and the formation of stable $(Mn,Cr)_3O_4$ spinel oxide compound [13]. In addition, the oxidation properties of stainless steel alloys can be influenced by microalloying. Particularly, the addition of elements that form very stable oxides at the oxide–metal interface, i.e., reactive elements, influence the growth rate, the composition, and the adhesion of the oxide layer [13]. The identification and the study of the critical elements that determine the oxidation properties are best achieved by investigating the initial stages of oxidation, which was exploited in this work. In Paper IV, the Nb alloying (0.2 at.%) of EN 1.4509 was shown to hinder the formation of SiO_2 at the oxide–metal interface, which also influenced the Mn to Cr ratio in the oxide layer.

Furthermore, oxidation is strongly affected by the composition of the oxidative atmosphere. Particularly, the oxidation mechanism for oxygen presented above (Fig. 2.6) is altered in the presence of H_2O that is evidently present in almost every application atmosphere (e.g., it is a reaction product of many combustion reactions) [34]. Under high-temperature moist conditions, the oxidation rates of stainless steel alloys are increased in comparison to dry atmosphere, which is largely due to the formation of volatile Cr-hydroxide compounds [13]. In contrast, under low temperature conditions pre-adsorbed H_2O results in kinetic hindrance of the oxide layer growth [Paper I].

2.4 Requirements for the oxide layer properties in solid-oxide fuel cell applications

Stainless steel alloys are needed in various industrial applications where different forms of corrosion are critical issues for the materials performance. The selection of a steel grade with an optimum composition for a particular application is important, since different grades are designed to sustain different forms of corrosion. This is because the alloy composition is the largest factor that affects the oxide layer composition, that determines whether the oxide layer remains protective or not. Energy conversion devices, such as combustion engines and fuel cells, are practical examples of applications where different forms of corrosion can occur. A common feature of these applications is that they include many auxiliary components such as fuel distribution and exhaust systems. Nevertheless, the corrosion requirements depend largely on the temperature, the chosen fuel, and its purity [35].

For example, Fig. 2.8 shows an automotive exhaust system where diverse constraints for materials in different parts are indicated [36]. Firstly, exhaust products contain several corrosive compounds of, e.g., C, Cl, N, S, and H_2O. Secondly, depending on the temperature of the section, these compounds can be in forms of gases or condensates [37]. Therefore, the operation conditions vary extensively between the high-temperature environment of the exhaust manifold next to the engine (i.e., hot end) and the acidic moist environment of the rear muffler at the cold end. For these reasons, the stainless steel grade with high oxidation resistance (high Cr content with Si or Al, e.g., EN 1.4509) is an optimal choice for the exhaust manifold, whereas Mo alloyed grades (e.g., EN 1.4521) are better suited to the moist corrosive conditions at the cold end.

FERRITIC STAINLESS STEEL IN AUTOMOTIVE EXHAUST SYSTEMS

COLD END
CRITICAL PROPERTY:
wet corrosion resistance

Rear muffler (400 °C)

Rear pipes (600 °C)

Front muffler (750 °C)

Catalytic converter (800 °C)

Increasing temperature

Front pipes (800 °C)

Exhaust manifold (950 °C)

CRITICAL PROPERTY:
oxidation resistance

HOT END
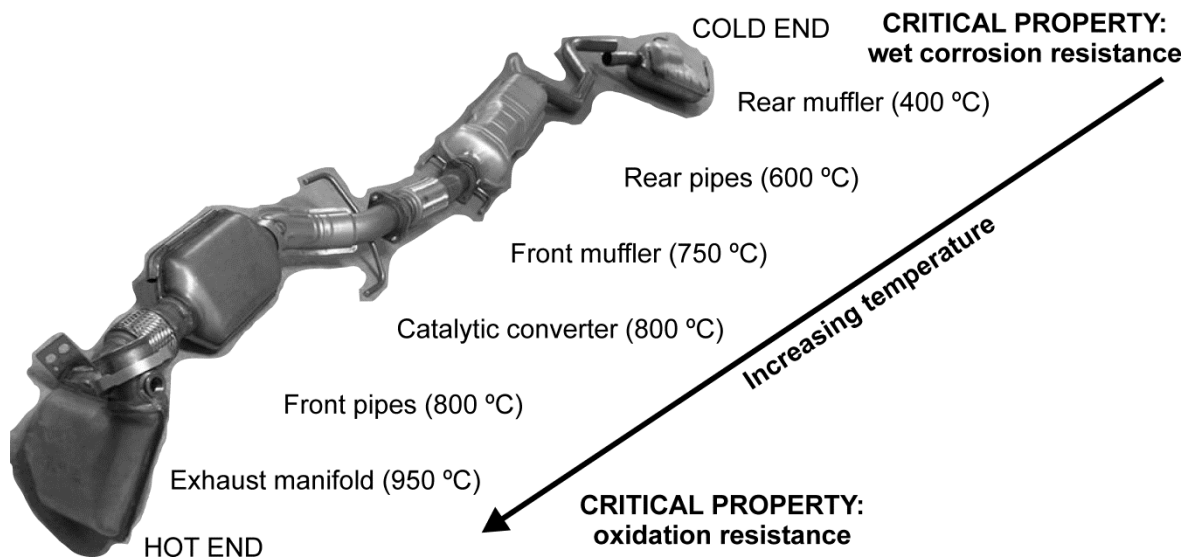
Fig. 2.8 – The diverse constraints for ferritic stainless steel materials in an automotive exhaust system. The photo by courtesy of J. Säynäjäkangas, Outokumpu Stainless Oy.

In practice, the chosen material is not the one with the highest operation performance but the cheapest material with sufficiently long service life. Today, the most widely used material in different parts of the automotive exhaust system is Ti microalloyed Fe–11Cr (m.%) with a lower degree of alloying than the ones presented above [37]. However, due to the tightening of the exhaust gas regulations, the operation temperature of the exhaust system has recently increased [36]. In addition, the demand to reduce the fuel consumption by reducing the vehicle weight has required the use of materials with higher corrosion resistance. Therefore, the use of cost-effective ferritic stainless steel grades, which have excellent oxidation resistance, is expected to further increase in the automotive industry.

An example of an application with particularly strict requirements for material selection is the interconnect plates of the SOFC, which is illustrated in Fig. 2.9 [38]. SOFCs are fuel flexible energy conversion devices that transform the chemical energy of fuel (e.g., H_2, natural gas) directly into electricity with high efficiency at high temperatures. Interconnects are required to separate individual cells in a fuel cell stack to obtain high power. They are part of the electrical circuit and exposed to air at the cathode and fuel at the anode side. Therefore, an interconnect material must obtain excellent electrical and high-temperature oxidation properties. On the other hand, electrical conductivity is not required for the other structural components of the SOFC [39].

FERRITIC STAINLESS STEEL IN SOFC INTERCONNECT APPLICATIONS

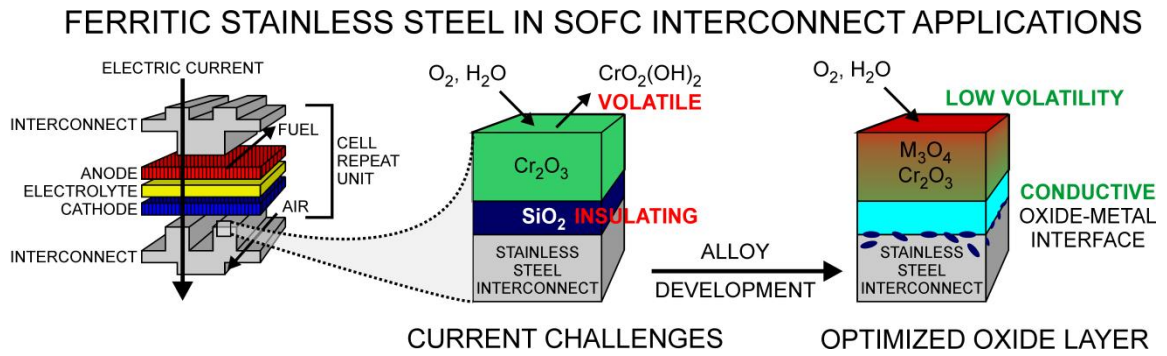Fig. 2.9 – Current challenges in the oxidation properties of ferritic stainless steels in solid-oxide fuel cell interconnect applications.

Due to development in the SOFC technology, the operation temperature has decreased down to 650 °C, and there is potential to go as low as 350 °C in the future [40]. Therefore, ferritic stainless steel alloys have become a strong choice for interconnect materials. This is largely because they have excellent intrinsic high-temperature oxidation and matching thermal properties with the other cell components [41]. However, the use of traditional ferritic stainless steel grades as interconnect materials presents serious issues that lead to decreased operation performance. The crucial challenges are the loss of electrical conductivity upon the formation of electrically resistive oxide sublayers (e.g., SiO_2, Al_2O_3) and the formation of volatile Cr compounds (e.g., $CrO_2(OH)_2$, CrO_3) that are detrimental to the electrochemical cell reactions [42,43].

To overcome these issues, new ferritic stainless steel alloys and alloy-coating combinations (e.g., coating with $(Mn, Co)_3O_4$ spinel oxide) have been developed [12]. For example, Mn alloying has been shown to be effective against the Cr volatilization, because of the formation of Mn-rich spinel oxide $(Mn,Cr)_3O_4$ on the surface. Electrical properties, on the other hand, can be enhanced by manufacturing alloys with low Si and Al concentration. Alternatively, the alloying with elements that have propensity for the formation of intermetallic compounds that bind residual Si or affect SiO_2 layer distribution has been shown effective. In Paper III, the excess Nb alloying induced formation of (FeNbSi)-type intermetallic Laves phase particles in EN 1.4509 (Fe–19Cr–(Ti,Nb)) alloy was investigated. The Si-rich Laves phase particles in the alloy were shown to favor the formation of non-uniform Si oxide layer. Furthermore, the formation of conductive Nb oxides at the oxide–metal interface instead of Si oxides was found to enhance electrical properties of this alloy [Paper IV].

Generally, the electrical properties of the stainless steel alloys have been unheeded in the traditional alloy development. However, there is a demand for cost-effective structural materials that have high electrical conductivity in a wide temperature range. Particularly, different types of fuel cells from proton exchange membrane (PEM) fuel cells operating at 50 °C [44] to the SOFCs described above require new or modified materials for interconnect (or bipolar) plates that maintain high performance during the application's service life. Promising, but much less studied, mechanisms to enhance conductivity of an oxide layer include careful alloying with elements that induce doping effects [45] or the incorporation of conductive metal particles into the oxide layer [46].

3   INVESTIGATION OF INTERFACIAL OXIDATION

This chapter describes the stainless steel alloys studied, experimental procedures, surface treatments, and central experimental techniques that were utilized in this work to investigate interfacial oxidation of ferritic stainless steel. The majority of the experiments were conducted in well-controlled UHV conditions, which enabled studies of initial phases of oxidation starting from an oxygen free metallic surface. PES allows analysis of different chemical states of elements at the surface and it was, therefore, chosen as the primary analysis technique. This chapter emphasizes the versatile exploitation of the PES method, including synchrotron radiation mediated PES, photoemission electron microscopy (PEEM), and different depth profiling methods.

3.1   Stainless steel samples

The studied polycrystalline stainless steel alloys were supplied by Outokumpu Stainless Oy (Tornio, Finland). The alloys were manufactured industrially using common steel-making procedures. Table 3.1 shows the bulk composition of the studied materials in both atomic and mass concentrations. The atomic concentrations are preferred in the text for convenience. The surface composition of the alloy can be substantially different from the bulk composition. Segregation of trace and minor alloying elements may take place particularly at elevated temperatures. Therefore, in addition to the main alloying elements presented in Table 3.1, many trace and minor alloying elements (P, S, V, Al, Cu, W, Mo, Sb, As, Sn, N, and O) were detected on the surface during the experiments.

Table 3.1 – Bulk compositions and designations of the ferritic stainless steel samples studied in this work in atomic and mass concentrations (balance Fe).

Papers	Alloy designation		Cr	Ni	Si	Mn	C	Ti	Nb
I, II	EN 1.4016, AISI 430, Fe–17Cr	at.%	17.0	0.20	0.50	0.40	0.17	-	-
		m.%	16.1	0.17	0.26	0.40	0.04	-	-
III, IV	EN 1.4509, AISI 441, Fe–19Cr–(Ti,Nb)	at.%	18.9	0.35	0.88	0.50	0.08	0.12	0.22
		m.%	17.9	0.37	0.45	0.50	0.02	0.11	0.38

3.2   Surface treatments of stainless steel materials

Well-controlled experimental conditions are the basis for the investigation of segregation and initial oxidation phenomena on surfaces. Requirements for such conditions include capability

to adjust precisely the pressure and composition of the surrounding gas atmosphere as well as the sample temperature. However, the strictest requirement is set by the demand to maintain the prepared surface free of any contamination during the course of experiments. In this work, three different UHV systems were employed for the experiments with the base pressures of the order of 1×10^{-10} mbar, thereby satisfying the requirements for well-controlled experimental conditions. All these systems were equally equipped with ion guns for sample cleaning purposes, gas-dosing devices for oxidation experiments, sample annealing possibilities, and electron spectrometers for PES measurements. In addition, these systems were modular, which facilitated installation of optional equipment for *in situ* surface treatments.

The PES measurements utilizing conventional, non-monochromatized Al Kα radiation ($hv = 1486.6$ eV) were carried out in a multi-technique surface analysis system, which has a hemispherical VG Microtech CLAM4 MCD LNo5 electron analyzer. The equipment has been described in detail elsewhere (see Ref. [47]). The PES measurements employing synchrotron radiation ($hv = 43$–1500 eV) were performed at the soft X-ray beamline I311 in the synchrotron radiation facility MAX IV Laboratory (Sweden) [48]. In short, I311 is an undulator beamline with a modified SX-700 monochromator and has two separate endstations. One is equipped with a hemispherical SCIENTA SES-200 electron analyzer and the other has an Elmitec spectroscopic photoemission and low-energy electron microscope (SPELEEM) III [49].

Fig. 3.1 illustrates the experimental procedures that were applied in this work to study surface phenomena on stainless steel materials. For the experiments, disk-shaped samples (9 mm in diameter) were initially cut from a sheet and polished to mirror finish. Then, a new sample was inserted into a UHV system where atmospheric impurities and native oxides were removed by cycles of 2.0 keV Ar^+-ion sputtering at 25 °C and subsequent annealing at 400–800 °C for 10 min. This cleaning procedure was repeated before each new experiment until the initial surface condition was restored. The chemical composition of the surface was analyzed by PES after each surface treatment.

```
                        ┌─────────────────────────────────────────────┐
                        │                NEW SAMPLE                   │
                        └─────────────────────────────────────────────┘
                │                     │
                │          ┌──────────────────────────────────────┐      ┌──────────────┐
                │          │ EX SITU OXIDATION – high oxygen activity │───▶│ EIS analysis │
                │          └──────────────────────────────────────┘      └──────────────┘
```

WELL-CONTROLLED ULTRA HIGH VACUUM ENVIRONMENT

Ar$^+$-ion sputtering

Annealing

In situ surface treatment

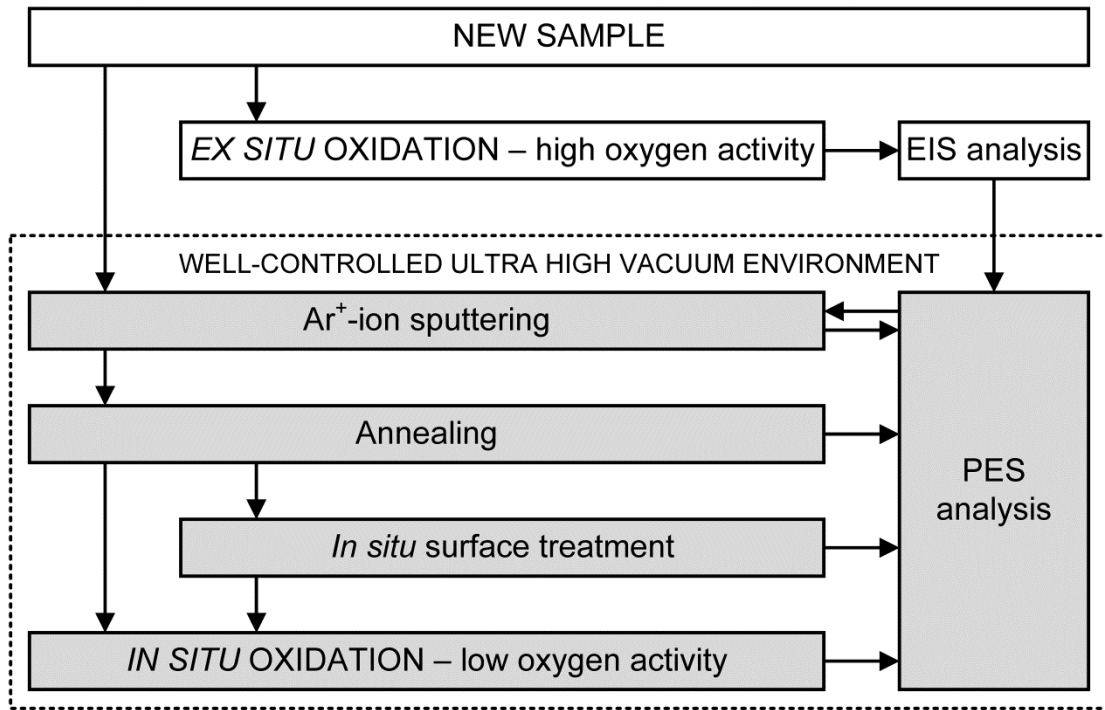IN SITU OXIDATION – low oxygen activity

PES analysis

Fig. 3.1 – The experimental procedures used in this work to study segregation and oxidation phenomena on ferritic stainless steel surfaces.

Surface segregation of alloying elements was studied by annealing the sputter-cleaned sample at selected temperatures up to 800 °C for 5 min and then allowing it to cool freely (within 1 h) to 50 °C before analysis. Short annealing times were applied to prevent undesired phase formation within the alloy during the experiments. In contrast, precipitation of intermetallic phases was intentionally induced by heat treatment in an Ar atmosphere at 800 °C for 120 h before analysis in Papers III and IV. Thermally induced segregation of alloying elements was applied as one surface treatment to modify the surface composition and to study influence of trace and minor alloying elements on initial stages of high-temperature oxidation [Paper II].

Influence of H_2O preadsorption on initial oxidation was studied at 50 °C [Paper I]. The reaction between a clean alloy surface and H_2O vapor was carried out in a small volume microchamber [47]. De-ionized H_2O was initially purified from dissolved gases by several freeze-pump-thaw cycles. Water saturated surface was then produced by backfilling the microchamber with 1.3×10^{-2} mbar H_2O for exposure of 10^7 L (1 L = 1.3×10^{-6} mbar s).

Physical vapor deposition (PVD) technique was employed to grow a Nb overlayer (layer thickness of 0.75 nm) on a Ti–Nb stabilized EN 1.4509 stainless steel alloy surface. The Nb/EN 1.4509 model system was applied to demonstrate the role of excess Nb to the initial

high-temperature oxidation at 650 °C [Paper IV]. An electron beam evaporator (EFM 3T from Omicron) with a Nb rod (99.9%, GoodFellow) was used as a Nb source. The Nb was deposited on the surface at room temperature and the sample was subsequently annealed at 650 °C for 5 min prior to the oxidation experiments.

Initial surface oxidation experiments were carried out *in situ* by backfilling the chamber with $1.3 \times 10^{-8} - 2.7 \times 10^{-6}$ mbar of O_2 (99.9999%) for exposures of 0.5–10,000 L. The sample temperature was maintained at the oxidation temperature of 50–800 °C during the exposure. At the low temperature of 50 °C the oxidation experiments were conducted as a function of exposure time [Paper I] whereas at temperatures above 300 °C constant exposure time and varied O_2 pressures were applied in order to regulate surface segregation during the experiment [Papers II–IV]. The low O_2 pressure was used in order to kinetically control the oxidation rate. From the thermodynamic point of view, oxidation at a low pressure of O_2 (low oxygen activity) favors the formation of thermodynamically most stable oxides, i.e., compounds that form at the oxide–metal interface (low effective oxygen activity) in ambient pressure conditions.

Oxidation experiments in ambient air (high oxygen activity) were carried out *ex situ* by placing the polished samples directly into a tube furnace at 650 °C for 30 min [Papers III, IV]. Then the samples were removed from the furnace and let to cool down freely followed by the EIS measurements and PES depth profiling. The results that were obtained using the high oxygen activity conditions were compared together with the results from the initial oxidation experiments.

3.3   Surface analysis by photoemission spectroscopy

3.3.1   Principles of photoemission spectroscopy

Photoemission spectroscopic techniques rely on the photoelectric effect, in which an atom absorbs a photon, and if the photon energy exceeds the binding energy of an electron, this photoelectron is emitted and the kinetic energy of the photoelectron depends on the photon energy. For solid surfaces, an additional amount of energy, the surface work function ϕ_s, is required to remove an electron from the surface to the vacuum level $E_{vac,s}$. In a photoemission spectroscopy measurement, a sample is illuminated with a (soft) X-ray source with a photon

energy *hν*, and the kinetic energy of the emitted electrons E_K is measured with an electron spectrometer. In a photoemission spectrum, the measured electron signal intensity is presented as a function of either kinetic or binding energy. If the work function of the spectrometer ϕ_{sp} is known, the binding energy of the photoelectron can be calculated:

$$E_B = h\nu - E_K - \phi_{sp} \, .$$ (3.1)

Fig. 3.2 illustrates the Equation (3.1) schematically and depicts the difference between the surface and the spectrometer work functions for a conductive sample that is grounded to the spectrometer. To measure binding energies of the photoelectrons accurately, the spectrometer needs to be calibrated according to well-known reference samples. In practice, measured spectra can be calibrated according to Fermi-edge ($E_F = 0$ eV) or known core-level peak, e.g., in this work the metallic Fe $2p_{3/2}$ photoemission peak was set to 707.0 eV [50].
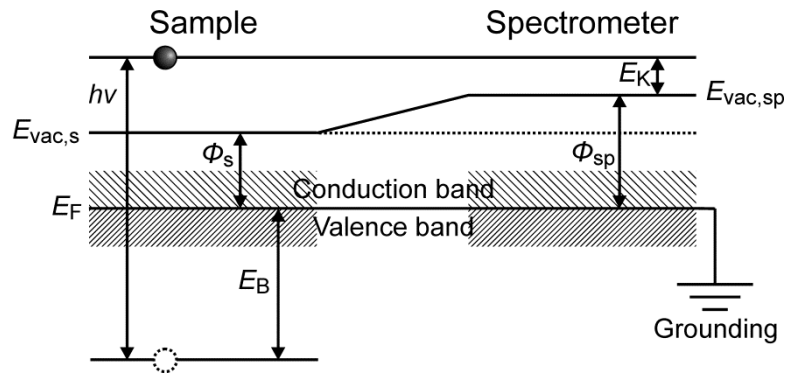

Fig. 3.2 – The influence of the spectrometer work function on the kinetic energy of a photoelectron that is emitted from of a metallic sample. (Adapted from [51].)

The electron configuration and the electron binding energies are characteristic for each element. The binding energies of electrons in an atom increase from weakly bound valence band electrons to the strongly bound core-level electrons, which are localized closer to the nucleus. The core-level electrons do not take part in the chemical bond formation, and, therefore, their binding energies can be used for elemental analysis of a sample. Moreover, the binding energies of core-level electrons are affected by the chemical environment of an atom, which is detected as small but measurable binding energy shifts [52]. This feature provides a means for analyzing, for example, different oxidation states of metals, which makes the core-level PES a powerful analysis method for surface oxidation studies of alloy surfaces. The analysis of the core-level photoemission data is discussed in detail in Chapter 3.4. In contrast,

the analysis of weakly bound valence electrons can be effectively applied to study bonding on the surface but the quantitative use of valence band spectra is more complicated in comparison to the core-level spectra [53]. In this thesis, PES refers to core-level photoemission spectroscopy that is also called as electron spectroscopy for chemical analysis (ESCA) or X-ray photoelectron spectroscopy (XPS).

After the photoemission of a core electron (Fig. 3.3(a)), the atom (or more precisely the ion) has an electron hole at the corresponding core-level. This excited state is unstable and therefore the excess energy must be released. There are two competing relaxation processes. The core-hole is filled with an electron from a higher energy level and the excess energy is released either by emitting a photon in X-ray fluorescence process (Fig. 3.3(b)) or by emitting an electron from a higher energy level in an Auger process (Fig. 3.3(c)). Since the Auger process causes electron emission, corresponding electron transitions show up in the PES spectrum. The analysis of these transitions can provide supplementary information to the PES analysis about the chemical compounds. A characteristic feature of the Auger electrons is that their kinetic energy does not depend on the photon energy but on the electron energy levels that take part into the Auger process (cf. photoelectrons). The photoemission peaks in the spectrum are denoted by the element and electron orbital that is involved in the photoemission process (e.g., O 1s) whereas the Auger electron transitions are denoted by the element and electron energy levels involved in the Auger process (e.g., O KL_1L_3).
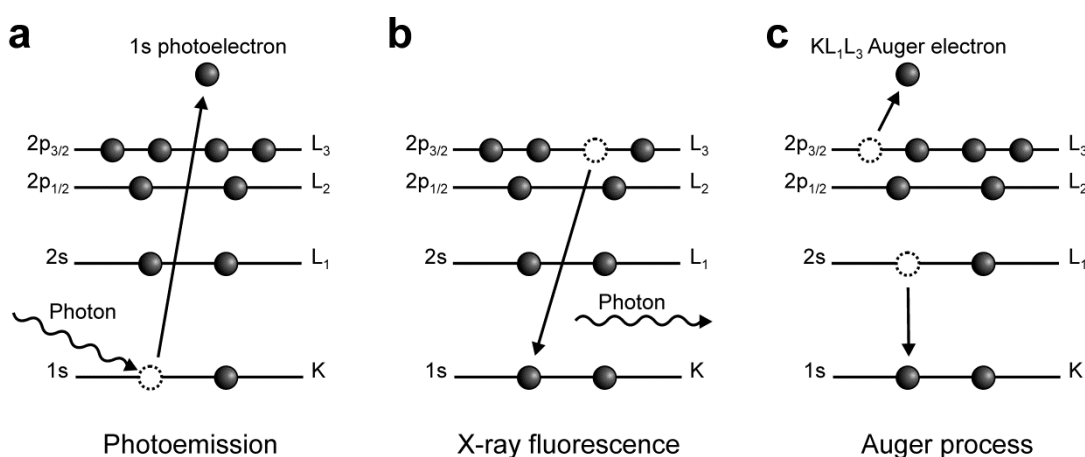

Fig. 3.3 – Illustration of the (a) photoemission process and the following competing relaxation processes: (b) X-ray fluorescence and (c) Auger process. (Adapted from [54].)

Fig. 3.4 shows a schematic illustration of the typical components required for a photoemission measurement. X-ray sources that were utilized in this work were a dual anode X-ray source

24

providing non-monochromatized Al Kα and Mg Kα radiation (hν = 1486.6 eV and 1253.6 eV) and a synchrotron radiation source (hν = 43–1500 eV). The kinetic energy of the photoemitted electrons can be measured with an electron spectrometer that consists of a lens system, a hemispherical electron energy analyzer, and an electron detector. The purpose of the lens system is to focus the photoemitted electrons and to retard the kinetic energy of the electrons for the hemispherical electron energy analyzer. The analyzer is typically operated at fixed analyzer transmission (FAT) mode, which allows only electrons at the fixed kinetic energy (e.g., 20 eV) to pass through the hemispherical part of the electron energy analyzer to the electron detector.
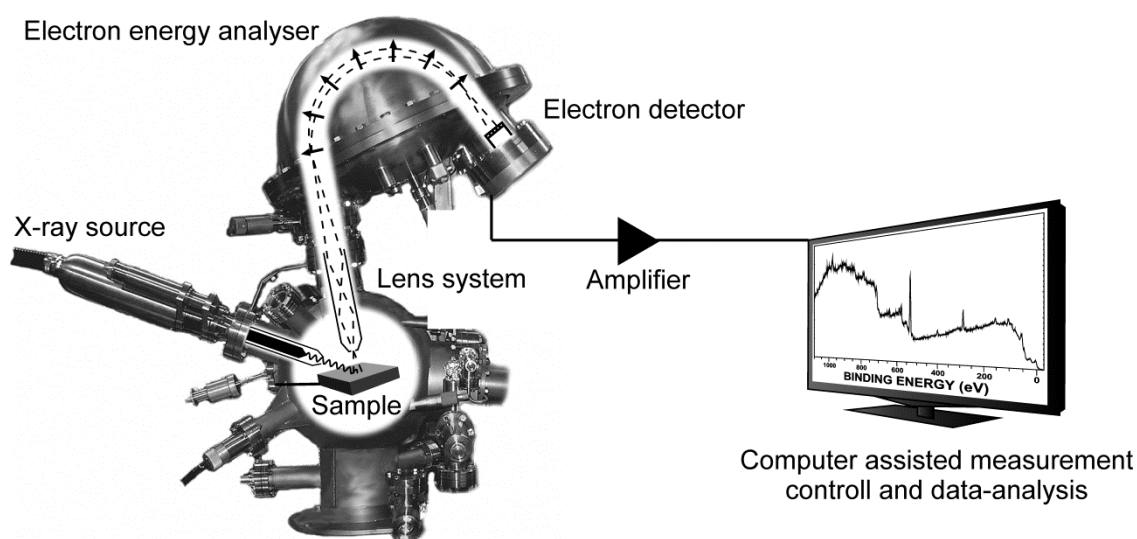

Fig. 3.4 – A schematic illustration of the typical components required for a photoemission measurement. The photo by courtesy of M. Hannula.

To obtain a PES spectrum, different retarding voltages over the spectrum energy range are applied to the lens system and the PES signal intensity is recorded by a computer. The electron detector can be an electron multiplier tube or more commonly a micro-channel plate (MCP) that consists of a matrix of separate detector channels. The MCP detectors can be, therefore, applied for imaging purposes with a suitable electron spectrometer. PEEM technique, that provides photoemission spectroscopy data with high spatial resolution, will be discussed in more detail in Chapter 3.4.4. In contrast, the analyzed surface area in a typical PES setup is large (~ 500 μm in diameter) in comparison to the average grain size of the studied stainless steel materials (~ 10 μm). Therefore, the results represent surface analysis over a large number of individual grains.

3.3.2 Surface and chemical sensitivity

The surface sensitivity of PES is based on the high probability for electrons to lose kinetic energy in inelastic scattering processes in solids. Inelastic mean free path (λ, IMFP) of an electron describes the average path length that an electron travels before losing kinetic energy in a scattering process. The IMFP value depends largely on the kinetic energy of an electron but only little on the solid material as shown in Fig. 3.5. The figure points out the surface sensitive electron kinetic energy range, which covers the typical kinetic energies of electrons, 100–1400 eV, in a PES measurement. The IMFP values in this range are 0.5–3 nm, which is equal to approximately 2–10 atomic layers. The kinetic energy of the photoelectrons can be affected by the photon energy and by the choice of the photoelectron transitions (core levels) that are used for the analysis [54]. Only photoelectrons that have not lost energy in inelastic scattering processes can contribute to the main peak intensity in the PES spectrum. In general, the PES information depth is given as 3 λ (about 10 nm), which corresponds to the depth from which 95% of the photoelectron main peak signal intensity originates [54]. Inelastically scattered electrons form a background to the spectrum. By analyzing this background, information depth of the PES analysis can be extended to 5–10 λ as discussed in more detail in Chapter 3.4.3. The PES is therefore particularly suitable for the analysis of passive oxide layers on stainless steel alloys, which have typical thickness of 2–3 nm.
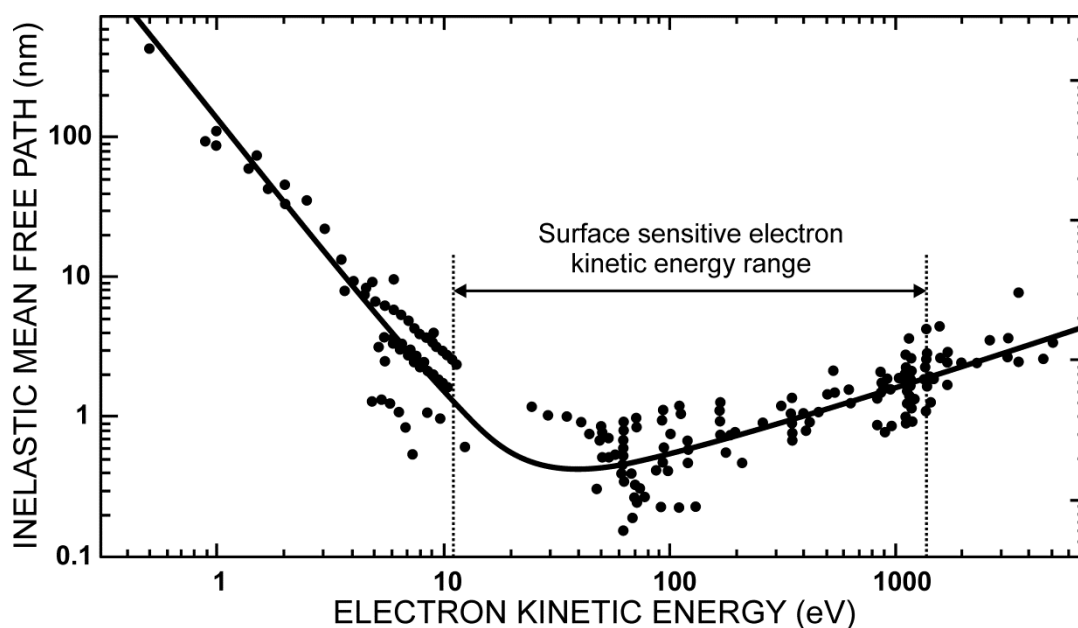

Fig. 3.5 – The inelastic mean free path as a function of kinetic energy of electron for various elements (adapted from [55]). The curve is the best fit with the experimental points and is also known as universal curve. The marked area points out the surface sensitive electron kinetic energies.

The elemental sensitivity of a conventional PES measurement (hv = 1486.6 eV) is typically expressed as 0.1 at.%, but in practice it is different for each element and, furthermore, it depends on the analyzed photoelectron transition. The intensity of the photoelectron peak is directly proportional to the photoelectric cross-section of the transition, which generally increases nonlinearly with decreasing photon energy as shown in Fig. 3.6(a) for the N 1s transition [54]. Fig. 3.6(b) demonstrates how elemental sensitivity can be enhanced by decreasing photon energy in the case of trace and minor alloying elements on EN 1.4016 alloy surface. It should be noted that the choice of the photon energy affects both elemental and surface sensitivity of the measurement.
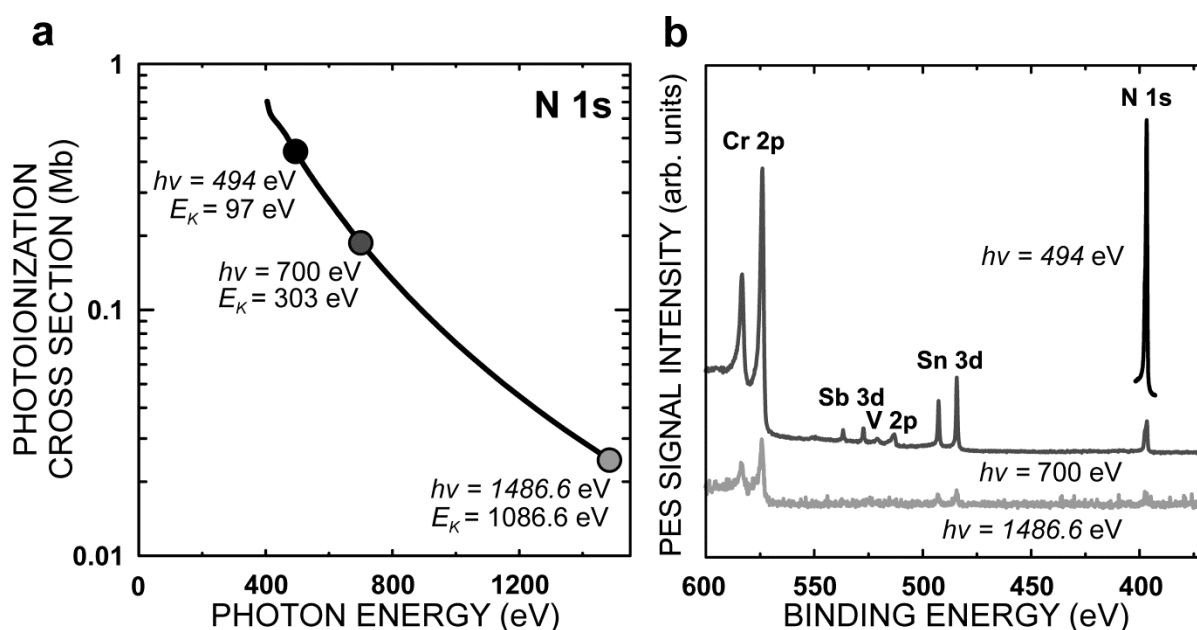
a

b

Fig. 3.6 – The influence of photon energy on the elemental and surface sensitivity. (a) Photoionization cross section as a function of photon energy for the N 1s core level (E_B = 397 eV) (adapted from [56]). (b) PES spectra of Fe–17Cr (EN 1.4016) sample at three different photon energies after sputter cleaning and subsequent annealing at 800 °C. The photon energy of 494 eV has the highest elemental and surface sensitivity to N 1s and it was, therefore, chosen for investigation of CrN surface compound formation in Paper II.

The sensitivity to distinguish different chemical compounds from each other (i.e., chemical sensitivity) by PES depends on the intrinsic peak width of the core-level, the chemical shift in core-level binding energy related to the chemical state (typically 1–5 eV) and the instrumental energy resolution of the PES measurement. The instrumental effects include the line width of the X-rays and the resolution of the electron energy analyzer. The line width of the X-rays can be affected by the choice of the light source and irradiation energy. For example, the line width of the Al Kα line is 0.85 eV [54], whereas the line widths of the soft X-rays at the

synchrotrons are typically below 0.10 eV [48]. To obtain the best energy resolution, instrumental parameters that affect the energy resolution need to be fine-tuned. However, the increased energy resolution comes at the expense of the decreased signal-to-noise ratio of the spectrum or longer data acquisition time. If the intrinsic peak width is broad, the ultimate energy resolution cannot provide any additional information. Therefore, total energy resolution needs to be optimized for each measurement.

The best surface and chemical sensitivity can be obtained by the use of soft X-ray synchrotron radiation. Synchrotron radiation is electromagnetic radiation that is emitted by electrons circulating at nearly the speed of light in a synchrotron storage ring. The synchrotron radiation spectrum covers a wide range of wavelengths (i.e., photon energies) from far infrared to hard X-rays. In modern synchrotrons, insertion devices are used to produce radiation with high brilliance (i.e., intensity). Insertion devices (e.g., undulators) are periodic magnetic structures that affect the electron trajectories to undulate, i.e. induce more radiation power. In comparison to laboratory X-ray sources, the brilliance of the synchrotron radiation is several orders of magnitude greater. The emitted radiation is directed to the studied sample through a monochromator, mirrors, and slits, i.e. through a beamline. The layout of the beamline I311 at the MAX IV Laboratory is illustrated in Fig. 3.7 [48]. The monochromator is applied to extract the desired photon energy from the broad spectral range of synchrotron radiation. The tunability of the photon energy is a strong advantage to the PES measurement, because the photon energy affects the elemental and surface sensitivity as described above.
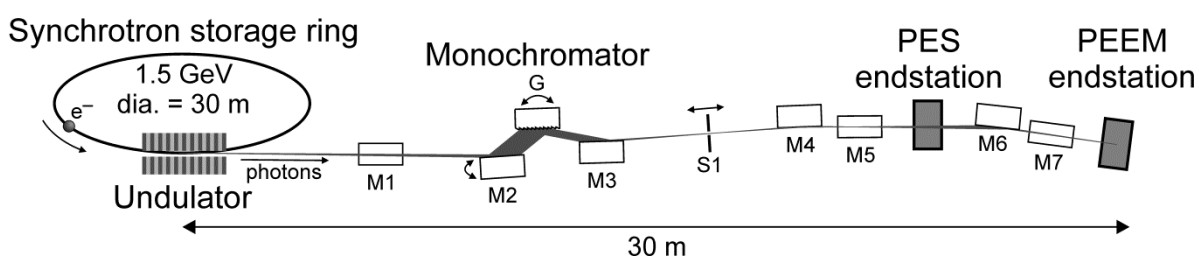
Fig. 3.7 – Schematic layout of the I311 beamline at MAXII synchrotron storage ring at the MAX IV Laboratory indicating positions of mirrors (M), exit slit (S1), and plane grating monochromator (G). The two endstations are operated one at a time. (Adapted from [48].)

The excellent brilliance of the synchrotron radiation can be traded with several improvements in the PES measurement. Firstly, it allows enhanced signal-to-noise ratio of the measurement, which decreases the data acquisition time. Alternatively, it can be used to improve energy resolution of the measurement by narrowing the incident X-ray line width. Secondly, high

brightness of the light source facilitates PEEM measurement by high spatial resolution together with maximized surface sensitivity, i.e. PES measurement from a small volume of substance on a surface [57]. Finally, high brightness with the development of applicable electron energy analyzers has enabled PES measurements at ambient pressures as high as 133 mbar (100 Torr) in contrast with the high vacuum requirement of the conventional PES measurements [58]. Therefore, ambient pressure photoelectron spectroscopy (APPES) has allowed PES measurements of the surfaces in the presence of gases and vapors that are relevant to industrial processes (e.g., catalysis) or environmental sciences (e.g., liquid water on a surface) [59,60]. For example, APPES has been utilized to study electrochemical cell reactions of SOFC under operation conditions (1 mbar H_2, 750 °C) [61].

Furthermore, the use of synchrotron radiation allows for new spectroscopic methods. In an X-ray absorption spectroscopy (XAS) technique, absorption of X-rays is measured as a function of photon energy. When the photon energy exceeds an X-ray absorption edge of an element, the X-ray absorption coefficient increases suddenly upon excitation of core-level electrons. The analysis of absorption edges provides information about the electronic and structural properties of the sample that can complement the information obtained from the PES measurement [62,63]. The structural sensitivity of the XAS measurement enables, for example, differentiation of metal oxides and interstitial compounds in stainless steels [64]. Technically, XAS and PES measurements can be conducted with the same instruments at a synchrotron radiation beamline. For example, Auger electron emission that follows the X-ray absorption is proportional to the absorption coefficient, and it can be utilized to measure XAS spectrum in a surface sensitive manner (i.e., Auger yield mode) [64].

In the analysis of buried layers and interfaces, e.g. oxide-metal interface of passivated stainless steel, the surface sensitivity of conventional PES may become a restrictive issue. However, the information depth of the PES measurement can be increased by the use of high incident photon energies, since the IMFP values increase with increasing electron kinetic energies, as is evident from Fig. 3.5 by extrapolating the curve to the higher energies. Nowadays, due to the development of electron energy analyzers capable of analyzing high electron kinetic energies, e.g. 4 keV, high kinetic energy photoelectron spectroscopy (HIKE) measurements with increased bulk sensitivity have become possible at the synchrotron radiation facilities [65].

3.4 Analysis of photoemission data

3.4.1 Chemical composition of the surface

A PES measurement starts by measuring a survey spectrum covering a wide binding energy range (e.g., 0–1100 eV) that includes photoelectron peaks of major and minor elements present. The survey spectrum is used for identification of the elements that are present on the surface and for the selection of the energy ranges for the high-resolution spectra. Typically, the most intense photoelectron peak of each element is chosen for the high-resolution spectrum, but in the case of overlapping spectral features, another peak can be selected. The exact binding energy values and the lineshapes of the photoelectron peaks are obtained from the high-resolution spectra and used for chemical state identification. Fig. 3.8 depicts a survey spectrum of oxidized Fe–17Cr sample, from which the spectral features of Fe, Cr, O and Ar were identified. The most intense Fe 2p, Cr 2p and O 1s photoelectron peaks were selected for the detailed analysis. The analysis of the Cr 2p high-resolution spectrum is shown in Fig. 3.8 inset. Annealing the sample at 327 °C was not efficient enough to remove residual Ar from the surface, which originated from the Ar^+-ion sputtering cleaning process prior to oxidation.
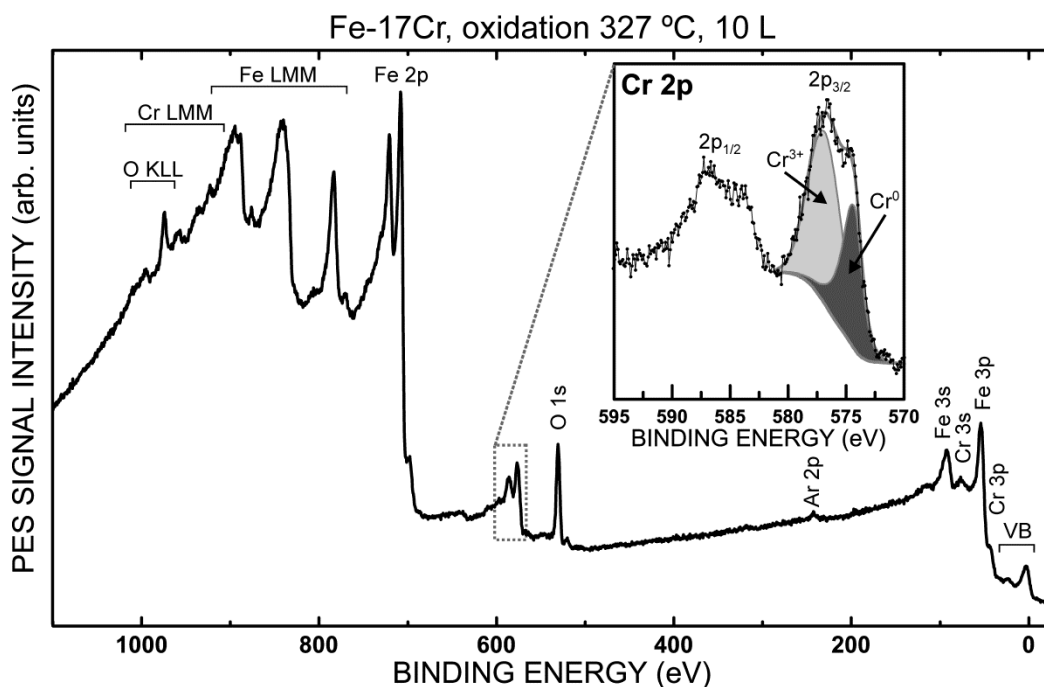

Fig. 3.8 – PES survey spectrum of Fe–17Cr (EN 1.4016) sample after 10 L oxygen exposure at 327 °C. The inset shows the analyzed Cr 2p high-resolution spectrum. The spectra were measured with non-monochromatized Al Kα radiation (hν = 1486.6 eV). (unpublished results)

The binding energy value of a photoelectron is affected by the initial and final state effects, which take place before and after the photoelectron excitation, respectively. The initial state effects are caused by the chemical environment of the atom (i.e., bonding) and they show up as small shifts in binding energy values (few eV) of the core level photoemission peaks, i.e. core level shifts (CLSs) [66]. The oxidation of a metal (i.e., loss of electrons) induces an effective positive charge on the atom, which increases the binding energy of electrons. Fig. 3.8 inset shows the CLS of 2.7 eV between oxidized Cr^{3+} and metallic Cr^0 [67]. In addition, the bonding environment of an atom on the top surface is different due to the missing neighbor atoms, which may give rise for a surface core level shift (SCLS) that has a typical magnitude of a few tenths of an eV. The measurement of such small energy shifts together with a sub-monolayer amount of substance requires the use of synchrotron radiation with enhanced surface and elemental sensitivity [57].

The final state effects may arise from shake-up and shake-off events and show up as satellite features in the spectrum [68]. In such events, photoelectron excites valence electrons to a previously unoccupied state or above the vacuum level. Thus, the satellite features always exist at the high binding energy (low kinetic energy) side of the primary photoemission peak [53]. The satellite features are characteristic to the chemical states of an element and can be, therefore, applied to complement the analysis. The identification of chemical compounds is typically carried out by comparing obtained values to the databases or reference data [50,69]. Yet, the binding energy values can be obtained by computational methods. The SCLSs of CrN surface compound on Fe–17Cr (EN 1.4016) were successfully estimated in Paper II using a thermo-chemical model that takes into account cohesive energies of compounds [70].

A photoelectron spectrum of a core-level is considered as a superposition of individual components (i.e., peaks) that correspond different chemical states of an element. To analyze the chemical states, a set of synthetic lineshapes is fitted to the spectrum by least-squares method after subtraction of a background and calibration of the binding energy scale. The background subtraction is required in order to remove the contribution of electrons scattered by inelastic processes from the primary photoemission peak area. The lineshapes and peak positions can be determined by analyzing reference samples with known composition or from the literature [71]. In the end, peak positions, full width at half maximum (FWHM) values, and peak areas are obtained from the analysis. As an example, Fig. 3.8 inset shows the

analysis of Cr $2p_{3/2}$ spectral region with a Shirley background and two components (Cr^0 and Cr^{3+}) with asymmetric Gaussian–Lorentzian lineshapes.

For many PES investigations, e.g. oxidation kinetic series, it is practical to determine the relative surface concentration of the chemical compounds. The determination is based on the measurement of photoemission peak areas I_x which are proportional to the amount of substance in the sample. However, the differences in the sensitivities between different photoemission peaks must be taken into account by atomic sensitivity factors

$$S = \sigma \lambda T A \,, \tag{3.2}$$

where σ is the photoionization cross-section of the analyzed photoemission peak, λ is the IMFP of photoelectrons in the sample medium, T is the electron energy analyzer's transmission function, and A is the product of the instrumental factors, e.g., sample area, that are usually constant within a measurement. Then, the relative concentration of element x in a sample can be expressed as

$$c_x = \frac{I_x/S_x}{\sum I_i/S_i}\,. \tag{3.3}$$

In the interpretation of the relative atomic concentrations, it is important to bear in mind that surfaces are seldom homogeneous and that different surface morphologies may yield the same result if the determination is based on the analysis of main photoemission peak areas only. Therefore, additional analysis methods are required to obtain information on the depth distribution of the elements. Different depth profiling methods will be discussed in Chapter 3.4.2. In addition, the information depth (3λ) depends on the kinetic energy of the photoelectrons, which is different for each photoemission peak when the measurement is conducted with fixed photon energy. To overcome this issue, it is possible to conduct the measurement with a constant electron kinetic energy at a synchrotron radiation facility that allows tunable photon energy.

As an additional feature in the analysis of the synchrotron radiation mediated PES data, in comparison with the analysis of the data obtained using a laboratory X-ray source, time-dependent variations in the photon flux must be taken into account by normalization of the spectra to the photocurrent or the storage ring current. Furthermore, the non-idealities in the

beamline optics may have a slight effect on the actual photon energy value. Therefore, a reliable calibration point for spectra is required after each change in the beamline parameters (e.g., change of the photon energy) and after an injection of a new electron beam into the storage ring.

3.4.2 Depth profiling

There are different ways to obtain information on the depth distribution of chemical compounds in the sample and they are all considered here as depth profiling methods. These methods can be categorized to destructive and non-destructive techniques. Depth profiling by alternating cycles of Ar^+-ion sputtering and PES measurement is a destructive method, in which the sample is bombarded with energetic Ar^+-ions to remove the surface layers. The sputtering rate is determined using a reference material with known thickness (e.g., Ta_2O_5(30 nm)/Ta). Due to the slow sputtering rate, this method is practical in the analysis of layer thicknesses less than 1 μm. This method is a valuable technique to study compounds at buried interfaces. Fig. 3.9(a) shows a depth profile of Fe–17Cr alloy sample that was oxidized for 30 min in ambient air at 650 °C. The depth profile provides the chemical composition and thickness of the oxide layer. Particularly, it reveals the formation of Si oxides and CrN compounds at the oxide–metal interface, which is illustrated by a schematic morphology of the oxide layer in Fig. 3.9(b). These results are in accordance with the results that were obtained in Paper II, where N was shown to be buried below the surface oxide layer upon initial high-temperature oxidation. When analyzing the depth profiles, some considerations should be taken into account regarding sputtering techniques in general. Firstly, sputtering rates of different species may vary. The sputtering rate of a metal is always higher than the sputtering rate of the corresponding metal oxides [72]. In addition, lighter compounds have higher sputtering rates than the heavier ones. If a sample consists of species with different sputtering rates, then preferential sputtering occurs. Secondly, the sputtering may induce chemical changes in the sample. For example, reduction of Nb_2O_5 oxide to NbO and NbO_2 oxides was reported in Ref. [73] upon Ar^+-ion sputtering. Therefore, non-destructive methods are required for a reliable analysis of the oxidation states.
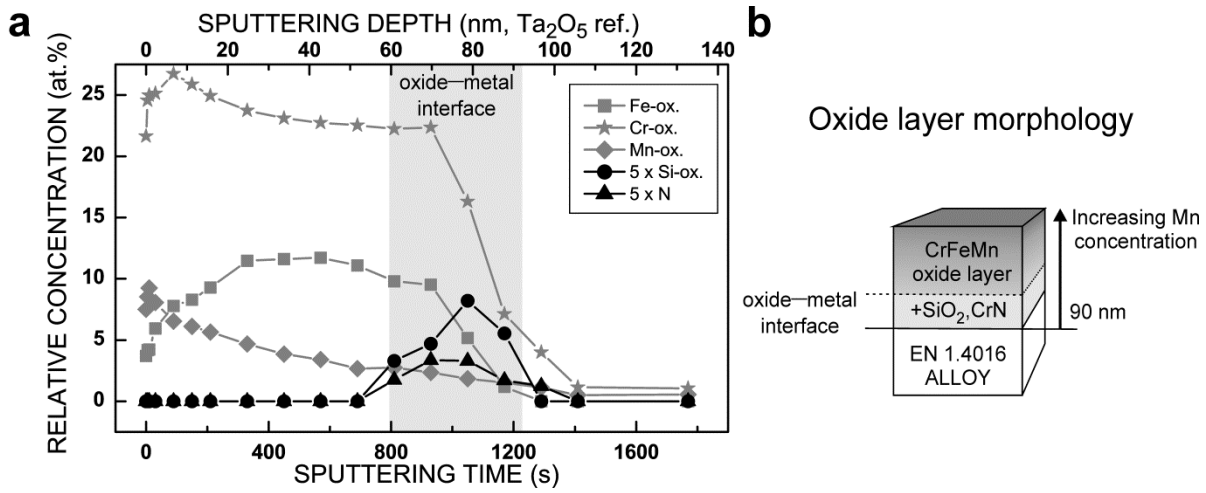
Fig. 3.9 – (a) PES depth profile of Fe–17Cr (EN 1.4016) sample after 30 min oxidation in ambient air at 650 °C. The depth profile shows oxidized components of Fe, Cr, Mn and Si. (b) The schematic oxide layer morphology. The formation of SiO₂ and CrN was found at the oxide–metal interface. (unpublished results)

Non-destructive PES depth profiling methods rely on the well-known inelastic scattering processes of electrons in solids. The attenuation of the photoemission signal by a homogeneous overlayer with thickness d obeys a Beer–Lambert equation

$$I = I_0 e^{-\frac{d}{\lambda \cos \theta}} ,$$ (3.4)

where I is the measured photoemission peak intensity, I_0 is the peak intensity without overlayer, λ is the IMFP value of the photoelectrons in the overlayer medium, and θ is the emission angle (i.e., the angle respective to the surface normal). By changing the angle of emission, e.g. by tilting the sample, surface sensitivity of the measurement can be varied. The information depth of the measurement is highest at normal emission ($\theta = 0°$) and decreases with $\cos \theta$. For example, at $\theta = 60°$ the information depth decreases to 50%. By measuring the PES data with different emission angles, information about the depth distribution of chemical compounds can be obtained, and in the case of layered structures, the depth distribution can be quantified based on Equation (3.4). This method is known as the angle resolved X-ray photoelectron spectroscopy (ARXPS), and it is particularly suitable for the analysis of thinfilms with thickness below 10 nm. For fast acquisition of the ARXPS data, special electron energy analyzers with large angular acceptance, which can record angular data without tilting the sample, have been developed [74].

Another way to obtain depth information without destroying the sample, is by utilizing the fact that IMFP of an electron depends on the kinetic energy [75]. When using a conventional laboratory X-ray source with fixed photon energy, it is sometimes useful to compare intensities of different photoemission peaks of the same element to obtain depth information. The higher the kinetic energy difference of the photoelectrons, the higher is the difference in the information depths. A more sophisticated method is to measure the photoemission spectra of a core-level peak as a function of photoelectron kinetic energy, i.e. by changing the photon energy, which requires the use of synchrotron radiation. Typically, such a measurement is applied to distinguish surface compounds from the bulk compounds by utilizing the electron kinetic energies less than 100 eV. However, nowadays it has become possible to utilize the high kinetic energy photoelectrons (e.g., 4000 eV) in PES measurement, which has enabled full depth profiling by such a method up to the depth of 20 nm [76].

The methods described above take into account only the intensity of the main photoelectron peak. However, the background of the photoelectron main peak (i.e., the high binding energy side) contains information about the depth distribution of an element because the background is formed by the photoelectrons that have scattered inelastically within the surface layers [77]. Qualitatively, an increase in the background intensity indicates that the emitting atoms are located below the surface. Low background intensity implies that the atoms are on the top surface. The quantitative analysis of the energy-loss background extends the analysis depth of PES to 5–10 λ (15–30 nm) and the method will be discussed in the following Section 3.4.3.

3.4.3 Inelastic electron energy-loss background analysis

The largest potential error in the analysis of the main photoemission peaks arises from the assumption that the depth distribution of the atoms is homogeneous within the information depth. Therefore, the interpretation of the analysis results may lead to an enormous error, unless the depth distribution of atoms is known. To emphasize the information that is contained in the background of the inelastically scattered electrons, Fig. 3.10 depicts three spectra of metallic Fe that originate from three different depth distributions of Fe atoms. In the analysis that only considers the main photoelectron peak intensities, all three Fe spectra produce the same analysis result because the main photoelectron peak intensities are the same. However, the real surface concentration of Fe varies between 0–100%.
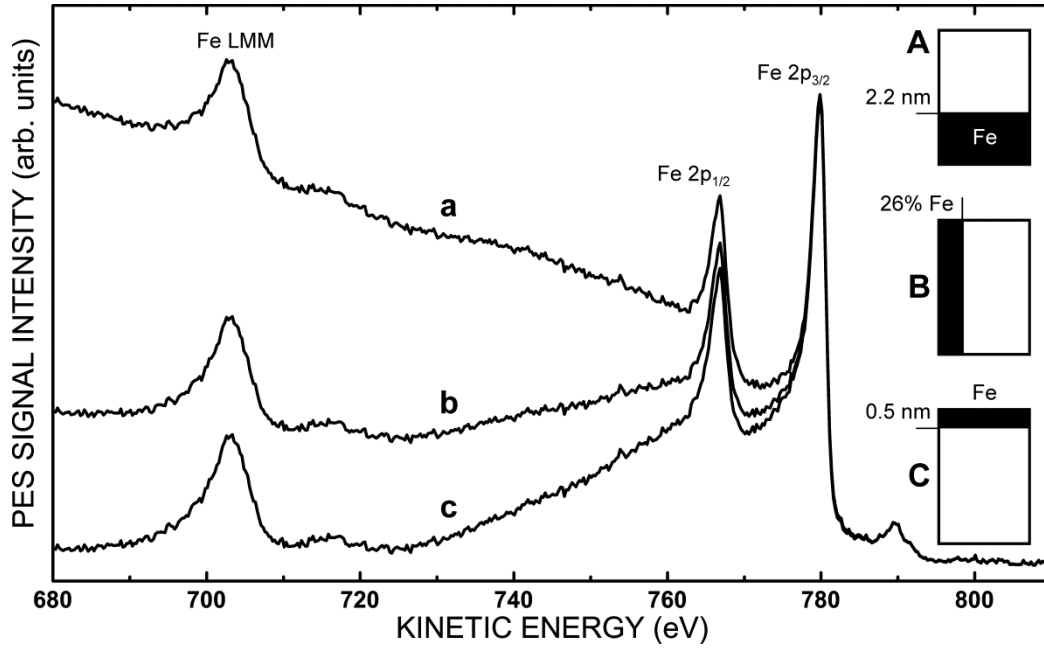
Fig. 3.10 – Three different metallic Fe morphologies (A–C) and corresponding PES spectra (a–c) modeled using the spectrum of the Fe 2p spectral region that was measured from the Fe reference sample. All three morphologies yield the same Fe $2p_{3/2}$ peak intensity but significantly different inelastic electron energy-loss background. (unpublished results)

The quantitative analysis of the photoelectron energy-loss background, which was used in this work, relies on an accurate description of inelastic electron scattering. The formalism behind the method has been developed by Tougaard et al., and the required analysis procedures are included into the 'QUASES' software package [78]. In short, the measured PES spectrum can be described by

$$ J(E_K, \Omega) = \int dE_0 F(E_0, \Omega) \int f(z) G\left(E_0, \frac{z}{\cos\theta}; E_K\right) dz , \qquad (3.5) $$

where F is the flux density of electrons excited from a single atom to a solid angle Ω with initial kinetic energy E_0, $f(z)$ is the concentration of the atoms at depth z, function G is the electron energy distribution as a function of travelled path z / $\cos\theta$ in the solid, and θ is the emission angle [79]. The total energy loss of an electron is influenced by the inelastic scattering events within the travelled path in the solid. Therefore, the energy distribution function G can be determined by the universal inelastic scattering cross-section function, which has been successfully applied in the studies of alloys and metal oxides [79].

In the analysis, a homogeneous reference sample with known $f(z)$ is measured in order to solve the primary excitation spectrum F. Then, the obtained F can be applied to the analysis of an unknown sample to solve $f(z)$. Reference samples are required to obtain fully quantitative analysis (i.e., the number of atoms in a unit volume) and to fine-tune the universal cross-section function that enhances the accuracy of the analysis. However, the analysis can be made without references by assuming that, after background correction to the measured spectrum J, the background of the primary excitation spectrum F must be of zero intensity. A typical error estimate for the quantification is $\pm$ 15% [80]. The analysis depth of the method is 5–10 λ and the depth resolution is $\lambda/3$. The depth resolution is considered as a capability to distinguish two different depth distributions if they differ significantly over this depth.

In the present work, the inelastic electron energy-loss background analysis of FeCr alloys was carried out by utilizing reference samples of metallic Fe, metallic Cr, oxidized Fe (Fe_3O_4), and oxidized Cr (Cr_2O_3) [81]. The calculations were performed using the 'Generate' program from the QUASES software package. The IMFP value of electrons is a critical parameter in the analysis and it depends on the kinetic energy of the electron as indicated in Fig. 3.5 and, furthermore, on the studied medium. Therefore, the exact IMFP values were calculated using the TPP-2M equation [82]. Fig. 3.11 demonstrates the analysis of Fe–17Cr (EN 1.4016) after 100 L oxygen exposure at 327 °C. For the analysis, a spectrum covering the energy range of the analyzed photoemission transitions (O 1s, Cr 2p, and Fe 2p) was first measured in the FAT mode of the energy analyzer (Fig. 3.11(a)). The required energy range for the background analysis should contain a sufficiently long background (about 100 eV) extending to the low kinetic energy side of the main photoemission peak. In addition, the analyzed energy region should not contain any extra photoemission peaks, unless they are included into the analysis. Then, the intensity of the spectrum was corrected for the energy dependence of the analyzer transmission, which was taken to be proportional to $E_K^{-0.7}$. Finally, the energy regions for each component were cropped into individual spectra and the background that originates from the photoemission transitions at the high kinetic energy side of the analyzed peak was subtracted from each energy region by assuming a linear background.
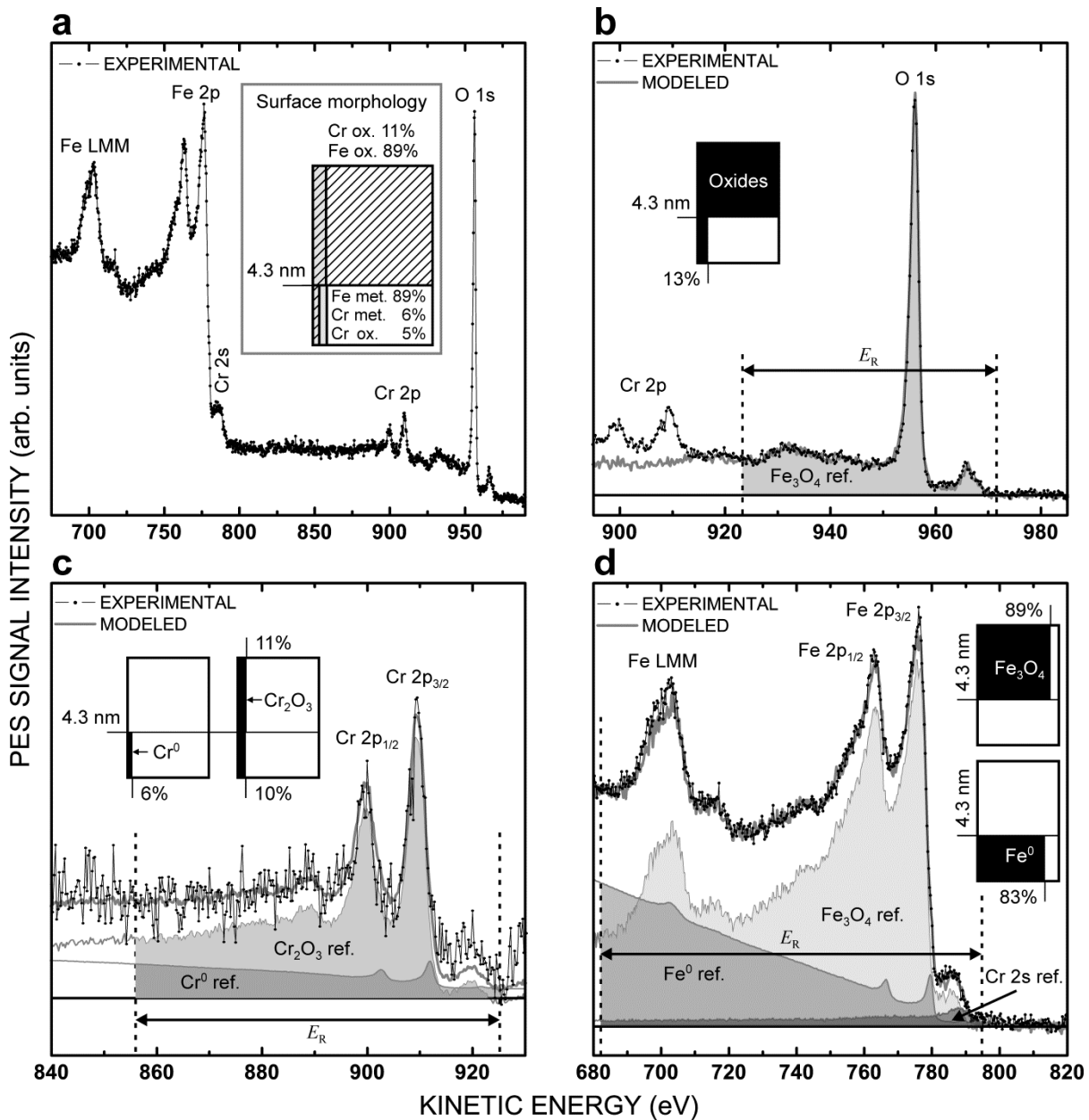
Fig. 3.11 – Inelastic electron energy-loss background analysis of Fe–17Cr (EN 1.4016) after 100 L oxygen exposure at 327 °C. (a) Survey spectrum showing all the analyzed photoemission peaks. (b) O 1s region modeled by the Fe_3O_4 reference (53.8 O^{2-} anions nm^{-3}). (c) Cr 2p region modeled by the metallic Cr^0 reference (83.3 Cr atoms nm^{-3}) and Cr_2O_3 reference (41.4 Cr^{2+} cations nm^{-3}). (d) Fe 2p region modeled by the metallic Fe^0 reference (84.9 Fe atoms nm^{-3}) and the Fe_3O_4 reference (40.3 $Fe^{2+/3+}$ cations nm^{-3}). The surface morphology and the relative atomic concentrations of the Fe and Cr species within the analysis depth, shown in the (a) inset, were obtained by combining the analysis of the O 1s, Cr 2p and Fe 2p regions within the analysis energy region E_R. (unpublished results)

Fig. 3.11(b–d) shows the analysis of O 1s, Cr 2p and Fe 2p energy regions. In the analysis, the spectrum for a given depth distribution and concentration of each atom or ion was modeled within the analysis energy region E_R. These parameters were then varied until the best agreement between the modeled and the measured spectrum was found. Analysis of the three

energy regions was combined in order to determine the location of the interfaces (e.g., the oxide layer thickness) and the relative atomic concentrations, i.e. to obtain the surface morphology as a result from the analysis that is shown in Fig. 3.11(a) inset.

3.4.4   Synchrotron radiation mediated X-ray photoemission electron microscopy

The modern synchrotron facilities with high-brightness tunable photon sources have allowed the development of core-level photoemission spectroscopic techniques that collect data from a smaller sample volume, i.e. with enhanced surface sensitivity and smaller analysis area, with sufficient signal level. This development has provided a means to analyze surface phenomena at a microscopic level by PES, which is of great interest in the investigation of technologically relevant materials. For example, the influence of precipitation and grain boundaries on surface phenomena on polycrystalline stainless steel alloys can be analyzed with a lateral resolution below the size of grains and individual precipitates [Paper III].

There are two ways to obtain high spatial resolution photoemission data at synchrotron radiation facilities [57,83,84]. Firstly, in the scanning photoelectron microscope (SPEM) the spatial resolution of 50 nm is achieved by the use of a focused photon beam and a scanning sample stage. In the SPEM, the resolution is determined by the photon beam focusing optics. Secondly, the spatial resolution of 40 nm can be achieved by the electron optics of the electron energy analyzer in an X-ray photoemission electron microscope (XPEEM), where the ultimate resolution is limited by the spherical and chromatic aberrations of the electron optics. Recently, surface analysis systems with XPEEM using an X-ray tube as the X-ray source have become commercially available reaching the resolution of 500 nm [85].

In the present work, synchrotron radiation mediated XPEEM measurements with an Elmitec spectroscopic photoemission and low-energy electron microscope (SPELEEM) III [49] were performed in Paper III. The SPELEEM instrument provides multi-technique measurements utilizing both the tunable electron and photon beam with different imaging modes for the analysis of surface composition and structure [86]. To obtain an XPEEM image, the electron energy analyzer is set to pass only electrons with selected kinetic energy to the image plane of the analyzer and the imaging is done by the electron optics. The XPEEM image is then projected to an MCP detector with a phosphorus screen, and recorded with a CCD camera. In XPEEM mode, an exit slit is set in front of the energy dispersive plane of the analyzer, which

filters the electrons with selected kinetic energy, and therefore, influences the energy resolution of the XPEEM image (typically 1 eV). Without the exit slit, the dispersive plane can be directly projected to the MCP detector to obtain a PES spectrum. This measurement mode is called µPES, because the electron optics can be used to select a small analysis area (e.g., 1 µm in diameter) from the sample for the PES spectrum. Normally, the µPES mode is employed to identify the chemical composition of the surface before time-consuming XPEEM measurements.
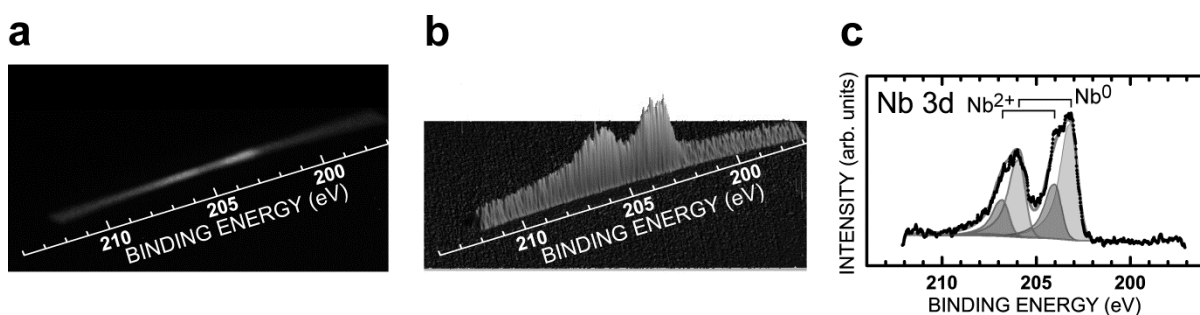

Fig. 3.12 – The analysis of the µPES spectrum of Nb 3d transition on EN 1.4509 after annealing at 650 °C recorded by MCP detector in energy dispersive mode. The (a) 2D and (b) 3D images of the intensity distribution. (c) The spectrum obtained by integrating the intensity perpendicular to the dispersion direction and after fitting of the synthetic components [Paper III].

Fig. 3.12 demonstrates the analysis of a µPES spectrum of Nb 3d photoemission transition. Fig. 3.12(a) shows the obtained spectrum as being displayed by the CCD camera image in 2D. The intensity variation is better illustrated in 3D image in Fig. 3.12(b). The final µPES spectrum in Fig. 3.12(c) was obtained by integrating the intensity perpendicular to the dispersion direction. The energy range of the spectrum is 15 eV, which is determined by the dimensions of the dispersive plane. Therefore, in order to identify all the photoemission peaks, the analyzer parameters need to be scanned across a wider energy range (cf. PES survey spectrum in Fig. 3.8). Particularly, the µPES spectrum of the valence band serves as a reliable calibration of the binding energy scale according to the Fermi-edge ($E_F = 0$ eV) for all the spectra.
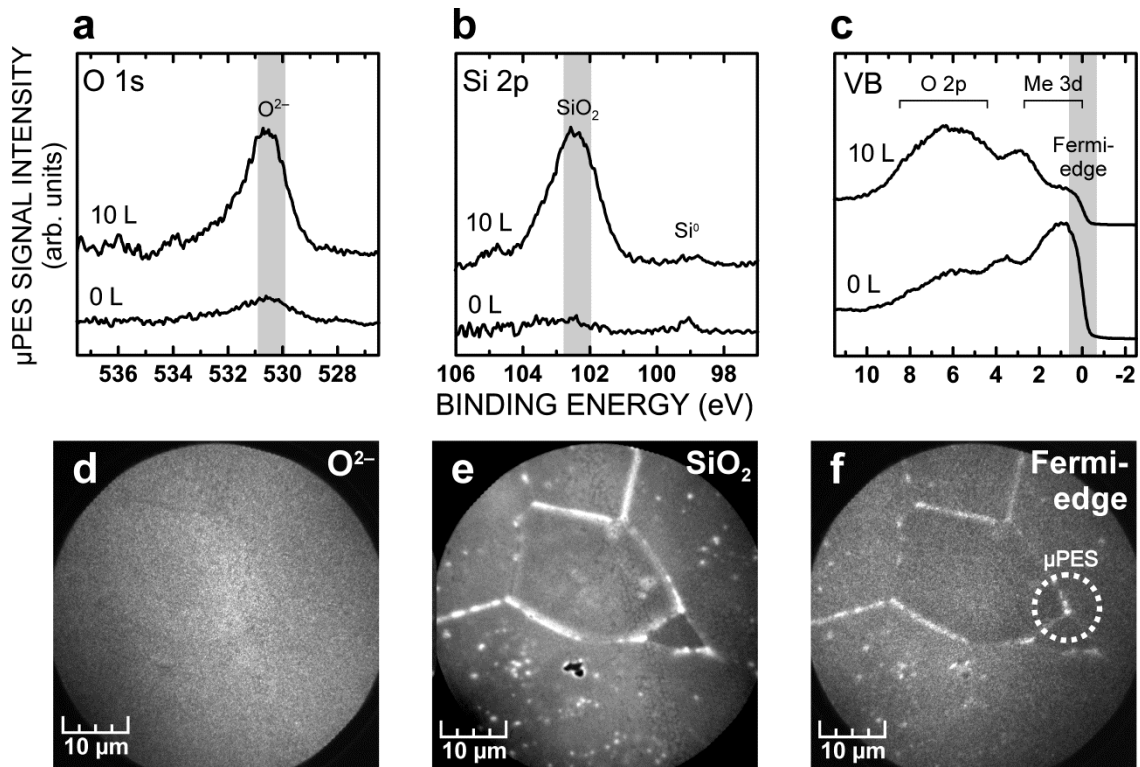
Fig. 3.13 – Initial oxidation of aged EN 1.4509 studied by SPELEEM. µPES spectra of (a) O 1s transition, (b) Si 2p transition and (c) valence band region before and after 10 L oxygen exposure at 650 °C. The analysis area of µPES spectra is indicated in (f) by a dashed line. XPEEM images of (d) O 1s transition, (e) Si 2p transition and (f) Fermi edge after oxygen exposure. The gray areas in Figs. (a–c) indicate the electron energy range that was used to give contrast in corresponding XPEEM images. (unpublished results)

Fig. 3.13 shows µPES and XPEEM results of the initial oxidation experiment on polycrystalline EN 1.4509 which contains Laves (FeNbSi)-type intermetallic precipitates. The comparison between the µPES spectra (a–c) and XPEEM images (d–e) reveals the complementary effect of the local information obtained by XPEEM versus averaged information of µPES. The µPES spectra of the O 1s (a) and Si 2p (b) transitions show the presence of oxygen and oxidized Si on the surface after oxidation. However, in the corresponding XPEEM images there is a strong contrast in the distribution of the oxidized species. The recorded image of the O 1s transition (d) corresponding to different metal oxides indicates that the whole surface is evenly oxidized, whereas the distribution of SiO_2 on the surface (e) is inhomogeneous and correlates with the location of the Si-rich Laves precipitates. The contrast in the XPEEM image of the Fermi-edge (f) arises from the metallic states of the elements on the surface. Surprisingly, the Fermi-edge image resembles the image of the oxidized SiO_2. The detected contrast in the Fermi-edge image is concluded to arise from the Laves phase precipitates, which are rich in Fe that does not oxidize at the studied conditions [Paper III].

41

3.5 Electrochemical impedance spectroscopy

Electrochemical impedance spectroscopy (EIS) allows the investigation of bulk transport properties within the materials and the electrochemical reactions at the interfaces [87]. It is often applied, together with other electrochemical methods, for corrosion studies of a material in a specific environment, since the corrosion reactions are electrochemical by nature [88]. Particularly, EIS has been utilized in the ongoing development of a theoretical model, namely the Point Defect Model, to explain the passivation of metals [89]. That is largely because the EIS method provides detailed information about the charge transfer and electrochemical reactions within the oxide films, coating and their interfaces, in a non-destructive manner. In this work, EIS was applied to study electrical properties of the thermally grown oxide layer on EN 1.4509 stainless steel alloy [Paper IV].

The EIS experiments in an aqueous electrolyte are typically performed in a three-electrode electrochemical cell that consists of a reference electrode, a counter electrode, and a sample as a working electrode. Impedance measurements can be performed as well with a solid electrolyte, but then the additional contribution of the charge transfer within the bulk electrolyte needs to be taken into account in the analysis [90]. In an EIS measurement, a small amplitude (e.g., 10 mV) AC signal is applied to the sample at a set potential and the impedance Z is measured as a function of AC signal frequency f. The measurement is done at a wide frequency range, typically from 1 mHz to 1 MHz. During the data acquisition, the system needs to be at a steady state. Therefore, the system is let to stabilize at the chosen potential before the measurement and the applied frequencies are optimized to shorten the data acquisition time. The impedance measurements in this work were performed using a computer-controlled potentiostat (Metrohm Autolab, Autolab PGSTAT12) with a frequency response analyzer module (FRA2).

Different relaxation processes in an electrochemical system respond to the perturbation signal at different frequencies, described by corresponding time constants $\tau = 1/2\pi f$ [24]. For example, relaxation processes that are related to corrosion of a material involving slow aqueous diffusion processes are typically slow and obtain therefore low characteristic frequencies (< 1 Hz), i.e. long time constants. Charge transfer reactions at the solid–solution interface are faster processes with higher characteristic frequencies (short time constants). The relaxation processes corresponding to fast charge transfer in an electrolyte solution take place

at high frequencies (> 10 kHz). For contrast, relaxation processes that take place in an atom after photoemission are extremely fast, corresponding to frequencies of 10^{14}–10^{16} Hz. The applied frequency range in the measurement can be, therefore, optimized according to the phenomena studied.
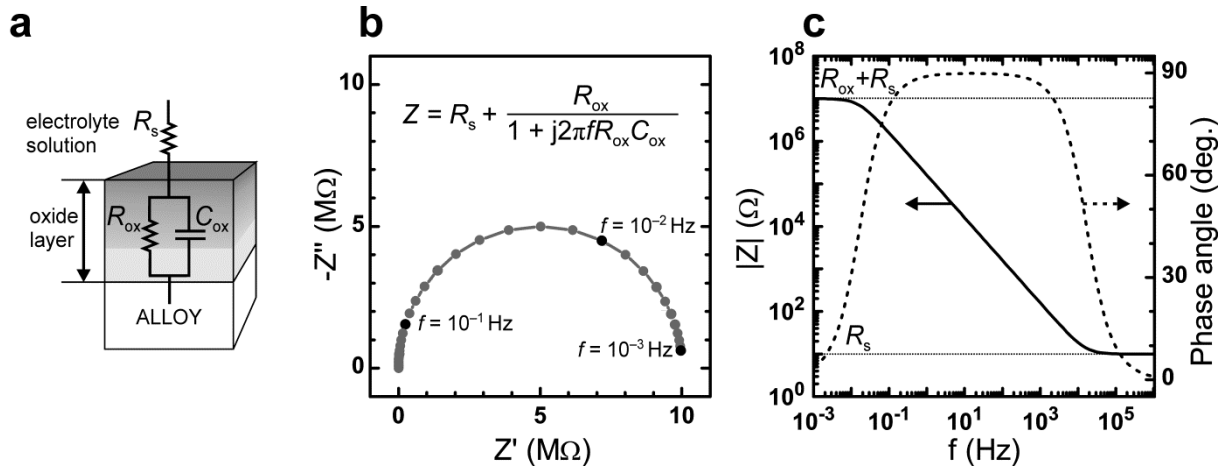

Fig. 3.14 – (a) Simple equivalent circuit for a thermal oxide layer. Calculated (b) Nyquist plot and (c) Bode plots for the equivalent circuit shown in (a) with R_s = 10 Ω, R_{ox} = 10 MΩ, C_{ox} = 1 μF. The equation of the impedance as a function of frequency is presented in (b) inset [24].

The interpretation of the impedance data is done by fitting with an adequate equivalent electric circuit that describes the physical system [91]. For example, the simplest equivalent circuit for an electrically resistive oxide layer on an alloy surface is presented in Fig. 3.14(a) [92]. The circuit consists of an oxide layer resistance R_{ox} and capacitance C_{ox} in parallel and an electrolyte solution resistance R_s in series. This circuit includes one Voight element (R and C in parallel), which corresponds to a time constant $\tau_{ox} = R_{ox}C_{ox}$ that describes the relaxation process related to the charge transfer within the oxide layer. In more complicated models a Voight element for each identified relaxation process can be included into the equivalent circuit to take into account e.g. solution–electrolyte and oxide–alloy interfaces or different sub scales in layered oxide scales [93,94]. However, the electrically most resistive subscale may dominate the total charge transfer resistance and complicate the distinction of the different phases in the analysis [89]. Besides resistance and capacitance, other circuit elements can be included as well. Commonly, a constant phase element (CPE) is used instead of pure capacitance to account for a non-ideal capacitive response of the real system [90]. However, as a rule for the analysis, the simplest circuit that describes the data adequately is often the best and helps to avoid over-interpretation of the data. Furthermore, it is a good practice to correlate obtained results with other experimental information. In Paper IV, EIS results of the

thermally grown oxide layer on EN 1.4509 alloy were correlated with the XPS depth profiling results.

There are different ways to present the impedance data. The Fig 3.14 shows modeled data for the equivalent circuit presented in (a) with R_s = 10 Ω, R_{ox} = 10 MΩ and C_{ox} = 1 µF as (b) a Nyquist plot (imaginary Z'' vs. real part Z' of the impedance) and (c) the corresponding Bode plots (impedance module |Z| and phase angle vs. frequency f). Different presentations of the data have different advantages for the data analysis. For example, the size of the semicircle in the Nyquist presentation indicates the total impedance of the studied system. The bigger semicircle may indicate increased corrosion/electrical resistance or growth of the oxide layer. For highly resistive systems, only an arc of the semicircle is observed, which is due to the low frequency limit of the measurement. The high frequency impedance is better expressed in the Bode plots. The impedance values at high frequencies approach the value of the solution resistance, which is insignificant compared with the total charge transfer resistance (R_{ox} + R_s) that is approached at the low frequencies. This low frequency limit of the impedance is equal to the electrical resistance, i.e. DC resistance. Furthermore, the minimum number of relaxation processes (time constants) taking place can be concluded from the number of semicircles in the Nyquist plot or from the number of peaks or related shoulders in the phase angle plot.

4 OPTIMIZATION OF THE OXIDATION PROPERTIES OF FeCr ALLOYS

In order to enhance the oxidation resistance of stainless steel alloys, the oxidation phenomena need to be investigated starting from the segregation of alloying elements and the initial stages of oxidation under an application specific environment. After the identification of the critical alloying elements or atmosphere constituents that determine the oxidation properties, focused development of alloys or surface treatments can be performed. This chapter summarizes the main results of this work related to the optimization of the oxidation properties of ferritic stainless steel alloys by controlled surface modification and microalloying.

4.1 Water adsorption induced kinetic control of the surface oxidation

One way to improve the operational performance of FeCr alloy surfaces under low temperature conditions is to modify its passive layer composition. The chemical composition of the surface controls its adhesion and reactivity towards adsorbates, which is crucial, e.g., to the corrosion and coating properties. For example, surface treatments that increase the Cr content of the passive layer improve the corrosion resistance and electrical conductivity of the alloy [44]. The analysis of the passive layers at the nanoscale requires surface sensitive techniques, which have been well developed and applied to study oxidation under aqueous environments [30,31]. However, only few studies focusing on the adsorption of O_2 on FeCr alloy surfaces have been conducted (e.g., [95]). Furthermore, oxidation is strongly affected by the oxidative gas atmosphere. In particular, the presence of H_2O vapor, that is evidently present in almost every application atmosphere, alters the oxidation mechanism in comparison to the oxidation under dry O_2 gas [34].

In this work, the formation of a passive oxide layer on the Fe–17Cr (EN 1.4016) alloy surface upon oxidation by low-pressure O_2 was studied at 50 °C [Paper I]. The low-pressure O_2 exposures allowed the kinetic control of the oxidation process. To investigate the influence of pre-adsorbed water on the passive film formation, the comparison was made between the surface that was sputter-cleaned and subsequently annealed at 400 °C and the surface that was further saturated with H_2O vapor. Fig. 4.1 shows (a) the average oxide layer thickness and (b)

the relative Cr concentrations within the oxide layer as a function of O_2 exposures for both surfaces. Furthermore, the surface morphologies resulting from selected exposures are shown in Fig. 4.2.
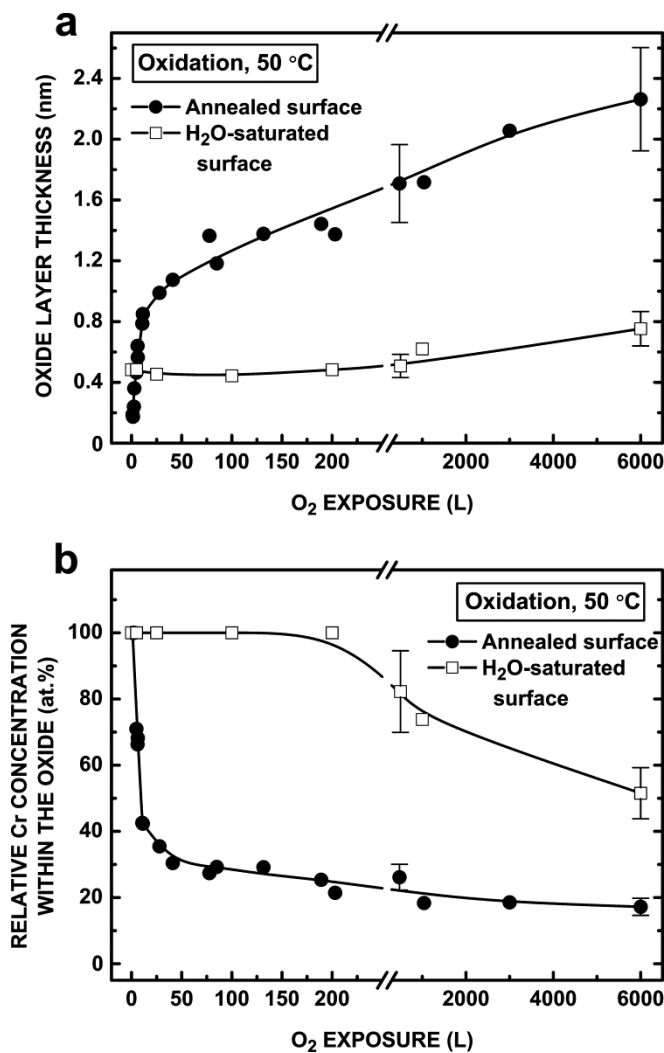

Fig. 4.1 – Inelastic electron background analysis results of the annealed and H_2O-saturated Fe–17Cr (EN 1.4016) surfaces after oxidation experiments at 50 °C: (a) The average oxide layer thickness as a function of the O_2 exposure as determined from the O 1s PES signal. (b) The concentration of Cr relative to all metal cations (Fe and Cr) within the oxide/oxyhydroxide as a function of the O_2 exposure as determined from the Cr 2p and Fe 2p PES signals. The solid lines shown are only to guide the eye. [Paper I]

The metallic (annealed) Fe–17Cr surface was highly reactive towards oxygen, which was indicated by the fast linear growth of the average oxide layer thickness up to ~0.8 nm (Fig. 4.1(a)). During this initial stage, the oxidation of Cr was strongly favored over the oxidation of Fe, which resulted in the enrichment of Cr in the oxide layer (Fig. 4.1(b)) and concurrent formation of the Cr-depleted oxide–metal interface depicted in Fig. 4.2(a). The following decrease in the oxidation rate was due to the transition from the nucleation and 2D growth of

the low-dimensional oxides to the 3D growth of the oxide layer (Chapter 2.3). Now, further oxidation required the ion diffusion through the oxide layer. It has been suggested that Fe cations have greater mobility than Cr cations and therefore the oxidation of Fe was supported during the latter stage [95]. Since the diffusion of ions at low temperatures is driven by the electric field that weakens rapidly with increasing oxide layer thickness, the oxide layer on the annealed Fe–17Cr surface reached its limiting thickness of 2.3 nm after 6000 L oxygen exposure, which indicated the passivation of the surface.
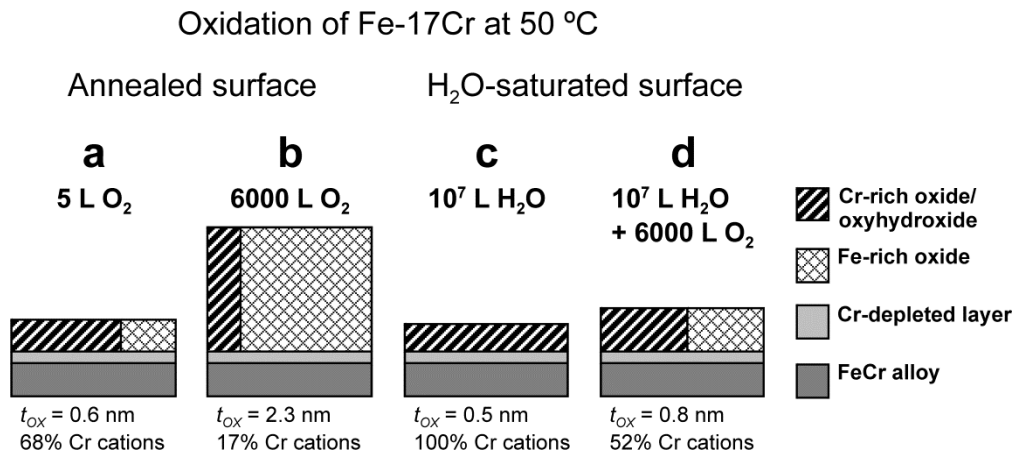

Fig. 4.2 – Surface morphology (including the oxide layer thickness t_{OX}) obtained by inelastic electron background analysis after the oxidation of the Fe–17Cr (EN 1.4016) surface at 50 °C: (a) the annealed surface after the O_2 exposures of (a) 5 L and (b) 6000 L, (c) the H_2O-saturated surface prior to any exposure to molecular oxygen, and (d) the H_2O-saturated surface after the O_2 exposure of 6000 L. The concentration of Cr within the oxide is given relative to all metal cations (Fe and Cr). [Paper I]

In contrast, the oxidation of Fe–17Cr surface was strongly influenced by H_2O preadsorption. Firstly, the H_2O exposure for Fe–17Cr resulted in a layer of Cr oxyhydroxides (CrOOH) with the limiting thickness of only 0.5 nm as depicted in Fig. 4.2(c). Thus, the FeCr surface reacted less readily with H_2O than with O_2 [96]. No Fe oxides formed, which is in sharp contrast to the H_2O adsorption on pure Fe [77]. Secondly, the H_2O preadsorption remarkably hindered further oxidation by O_2, which is clearly seen by comparing oxide layer morphologies with the same O_2 exposure in Figs. 4.2(b) and (d). Furthermore, the oxidation of Fe was detected only after 500 L O_2 exposure on H_2O saturated surface. It was concluded that the H_2O adsorption induced enrichment of Cr, and the strongly bound hydroxyl species on the surface hindered the ion diffusion through the oxide layer. Therefore, the controlled hydroxylation of FeCr alloy surfaces can be utilized to yield a Cr-rich passive layer with enhanced corrosion properties but also as a surface pretreatment for functional thin films, e.g., silane films, that bond with the surface via hydroxyl groups [97,98].

4.2 Role of excess N on the high-temperature interfacial oxidation

The enhanced properties of advanced ferritic stainless steel grades are achieved through careful optimization of the alloy composition, often involving microalloying and trace elements. The influence of these elements is particularly crucial to the interfacial phenomena under high-temperature conditions where they may become rapidly enriched to the surfaces through segregation and oxidation phenomena [34]. Therefore, microalloying with the elements (e.g., Si, Al, Ce) that form stable oxides at the oxide–metal interface or surface treatments that promote the formation of the Cr-rich oxide layer can be utilized to improve the oxidation resistance at high temperatures. On the other hand, the undesired enrichment of trace elements (P, S, Sn, Sb…) may lead to reduced adhesion, and eventually, to the spallation of the oxide layer (Chapter 2.2).

The segregation of minor alloying elements and their influence on initial high-temperature oxidation on Fe–17Cr (EN 1.4016) were studied at temperatures up to 800 °C in Paper II. At temperatures below 350 °C, the surface composition corresponded closely to the bulk composition of the alloy (Fig. 2.4(a)). When the temperature was increased, the surface enrichment of P, As, and other trace elements was detected. However, the most prominent was the cosegregation of Cr and N on the surface [19].

Fig. 4.3 shows the complex evolution of N 1s PES spectra as a function of annealing temperature. The peaks originating from three clearly distinguishable forms of nitrogen were assigned to interstitial nitrogen in solid solution (N in sol. peak at 397.54 eV), three-dimensional CrN precipitates (CrN,b peak at 397.02 eV) and a two-dimensional CrN surface compound (CrN,s peak at 396.68 eV). The detected binding energy shift between two- and three-dimensional CrN compounds (–0.34 eV) was concluded to arise from the SCLS of undercoordinated nitrogen atoms, which was in close proximity to the calculated value of –0.21 eV obtained by a thermo-chemical model. Fig. 4.4 depicts the surface morphologies of the samples after annealing at 327°C (Fe–17Cr, 0 L) and at 800 °C (N/Fe–17Cr, 0 L). The surface enrichment of Cr is due to the cosegregation of Cr and N and the thermally induced segregation of Cr is evident on the N/Fe–17Cr sample. The analyzed thickness of the CrN surface layer (0.12 nm) was in good accordance with the literature [19]. The impact of the cosegregation of Cr and N versus the thermally induced segregation of Cr was discussed in Chapter 2.2.
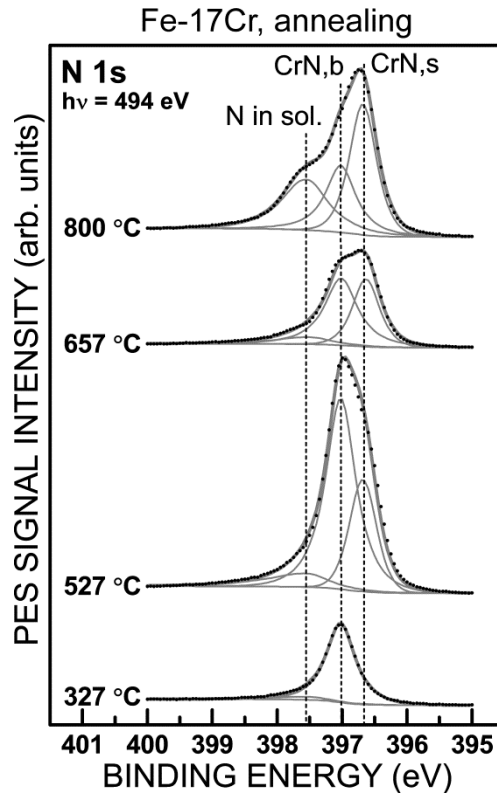
Fig. 4.3 – N 1s PES spectra of Fe–17Cr (EN 1.4016) after annealing at 327–800 °C in UHV. The spectra were recorded using photon energy of 494 eV. [Paper II]

The influence of the CrN surface compound on the initial stages of oxidation at 327 °C was studied by comparing the oxidation of surfaces that were pre-annealed at 327 °C or at 800 °C. Furthermore, the initial oxidation of the N/Fe–17Cr was studied at 800 °C. Fig. 4.4 presents the evolution of surface morphology upon oxidation. After oxidation at 327 °C, an Fe-rich mixed oxide layer developed on both surfaces. The presence of the CrN on the N/Fe–17Cr surface was shown to promote the selective oxidation of Cr initially, but the effect decreased towards higher O_2 exposures. However, the nitrogen was buried below the surface oxide layer, yet it had little effect on the oxidation rate. The fast initial formation of Cr-rich oxide layer is of great importance in applications involving high-temperature conditions with low oxygen activity.
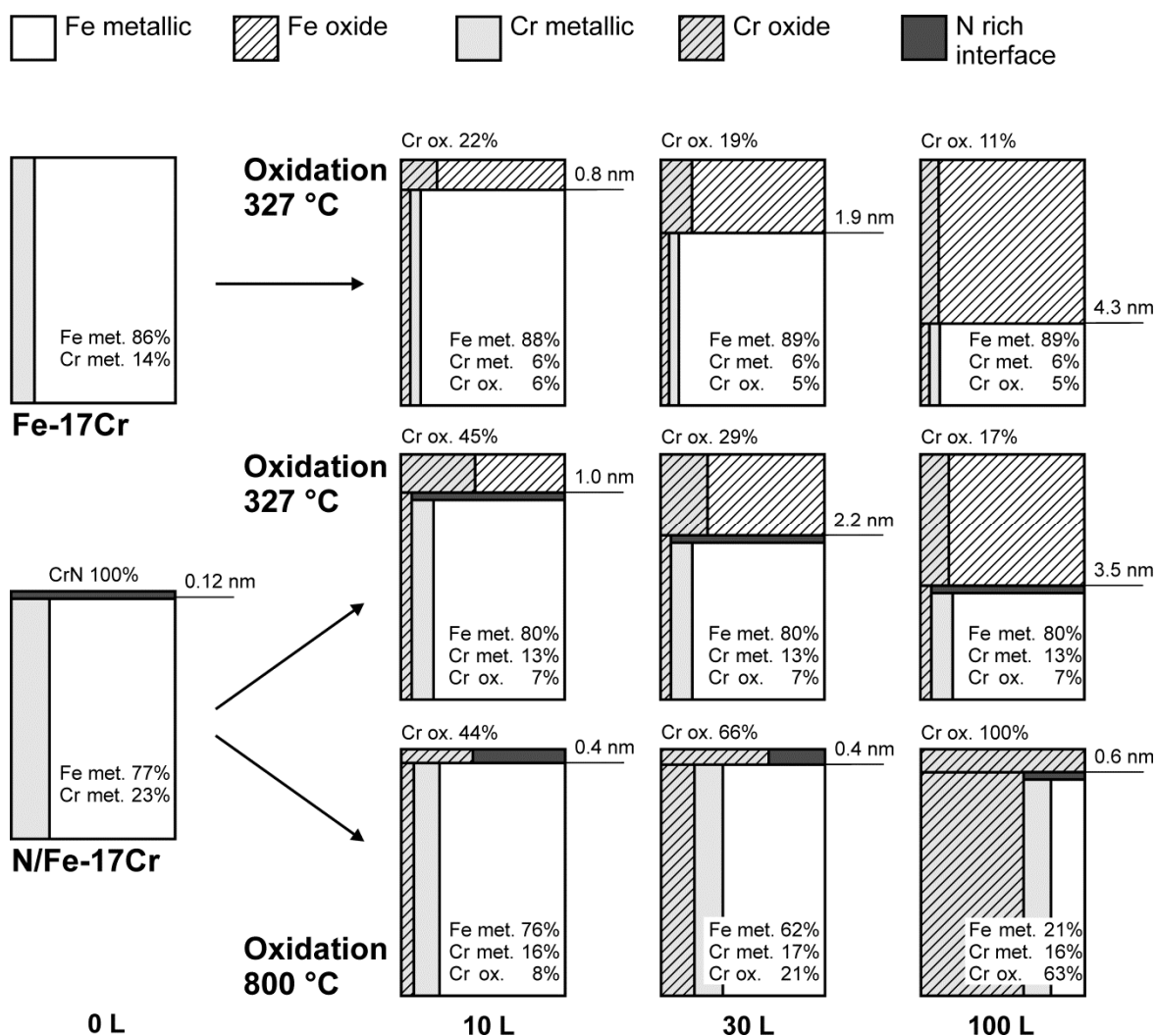
Fig. 4.4 – Inelastic electron background analysis results of Fe–17Cr and N/Fe–17Cr (EN 1.4016) after O_2 exposures of 0–100 L at 327 °C and at 800 °C. The morphology models represent cross-sections of the surface. [Paper II]

The oxidation was significantly different at 800 °C. In contrast to oxidation at 327 °C (cf. also to the oxidation at 50 °C in Fig. 4.2), Fe oxides did not form at 800 °C because the formation of Cr_2O_3 is thermodynamically more favorable and the thermal diffusion of Cr is sufficiently rapid to support it. Moreover, internal oxidation of Cr was detected within the near surface region, which is supported by the higher diffusion rate of oxygen in the FeCr alloy at 800 °C than that of Cr [18]. However, the surface and near-surface Cr_2O_3 were expected to coalesce at later stages of oxidation, producing a thick, protective oxide layer. In addition to Cr_2O_3, the oxygen-induced surface segregation and preferential oxidation of Si was detected at 800 °C (included in the oxide layer, but not indicated in Fig. 4.4). Both Si and N compounds were shown to locate at the oxide–metal interface of this alloy upon 30 min oxidation in air at 650 °C (Fig. 3.9), which is in excellent accordance with the initial oxidation experiments.

4.3 Influence of Nb microalloying on high-temperature oxidation

Nb is a strong carbide former and therefore small amounts of it is added to stainless steels to prevent unwanted precipitation of Cr with C [4]. In addition to carbides, Nb can form more stable oxides than Cr (e.g., NbO in Fig. 2.5). These oxides are located at the oxide–metal interface of FeCr alloys, together with other stable oxides, such as SiO_2, affecting the transport of ions to the oxide layer. Furthermore, at high temperatures Nb has a propensity to the formation of an intermetallic Fe_2Nb-type Laves phase [8]. These phenomena are interdependent and strongly affected by the exact alloy composition, the temperature and the atmosphere.

Recently, Nb alloying has been shown to have beneficial effect on the electrical properties of ferritic stainless steel alloys in SOFC interconnect applications (Chapter 2.4). Firstly, Fe_2Nb-type Laves phase particles can incorporate some residual Si from the alloy solution, and thus, hinder the formation of an electrically resistive SiO_2-rich subscale [12]. Secondly, the electrical conductivity of Nb oxides is comparable to that of Cr_2O_3, which is a p-type semiconductor with appropriate electrical properties for the interconnect applications [99,100]. Since both Nb and Si form oxides at the oxide–metal interface, competition for interfacial oxidation is expected but not yet revealed in the earlier studies. Besides, Froitzheim et al. have shown that extensive Nb alloying results in an undesirably high growth rate of the oxide layer [101]. In contrast, the Si addition has a well-known feature of improving the high-temperature oxidation resistance of the FeCr alloys [33].

In this work, the interfacial oxidation of Nb and Si on Laves phase forming Ti–Nb stabilized ferritic stainless steel (Fe–19Cr–0.9Si–0.2Nb–0.1Ti (at.%), Fe–19Cr–(Ti,Nb), EN 1.4509) was studied at 650 °C focusing on the alloy performance as a SOFC interconnect material [Papers III and IV]. The precipitation of the intermetallic Laves phase in the alloy was induced by heat treatment, i.e., aging, in an Ar atmosphere at 800 °C for 120 h. The higher temperature of the heat treatment in comparison to the selected temperature for oxidation experiments promoted the precipitation process, which was significantly slower at 650 °C and, therefore, avoided in the oxidation experiments [102]. However, the temperature of 650 °C was high enough to induce the surface segregation of Nb as shown in Fig. 2.4(b), whereas the segregation of other microalloying elements (e.g., Ti) was observed insignificant. In the investigation, a comparison was made between a heat-treated sample (denoted as "AGED")

51

and a sample that was not heat-treated, i.e., the sample did not contain the Laves phase ("NOT-AGED" sample).

Fig. 4.5 depicts the microstructure of the AGED sample and Table 4.1 presents the energy-dispersive X-ray spectroscopy (EDS) analysis results of the marked positions (A–D). The formation of (FeNbSi)-type Laves particles (white particles at the position A) occurred during the heat treatment, whereas other precipitates, Nb(Fe)-type carbides and TiN, originated from the manufacturing processes of the alloy [102]. Note that the majority of Si (0.8 at.%) remained in the ferrite matrix, albeit some Si was enriched into the Laves particles. Therefore, these Laves particles were shown to bind more effectively free Nb than Si from the solution.
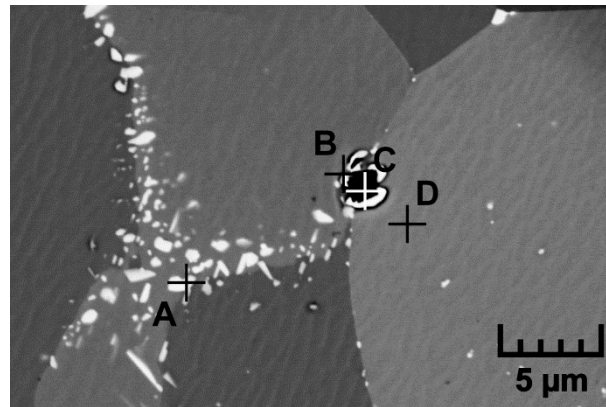

Fig. 4.5 – A FESEM micrograph of EN 1.4509 (Fe–19Cr–(Ti,Nb)) aged at 800 °C for 120 h. The marked positions indicate EDS analysis areas. [Paper III]

Table 4.1 – EDS analysis results in atomic-% of the positions indicated in Fig. 4.5. The interaction area (3 μm^2) is indicated by the size of the symbol in Fig. 4.5. [Paper III]

AREA	Fe	Cr	Si	Nb	C	N	Ti	PRIMARY PHASE
A	57.8	9.5	8.0	24.7	-	-	-	Laves
B	52.3	12.8	0.6	11.7	20.5	-	2.1	Nb(Fe)C
C	1.3	1.1	-	3.6	-	45.4	48.6	TiN
D	80.5	18.7	0.8	-	-	-	-	Ferrite (α)

The oxidation experiments for the NOT-AGED and AGED samples were first conducted in ambient air (i.e., high oxygen activity) at 650 °C. Fig. 4.6 presents PES depth profiles of the oxide layers showing the oxidized components of Fe, Cr, Mn, Si, and Nb. Both oxide layers had a typical composition for the studied FeCr alloy: the Cr,Mn-rich outer scale and the Cr-rich subscale [103]. The detected Fe oxides were expected to become converted into the thermodynamically more favorable species (e.g., $(Mn,Cr)_3O_4$ and Cr_2O_3) with increasing oxidation time. Furthermore, Si and Nb oxides were located at the oxide–metal interface.
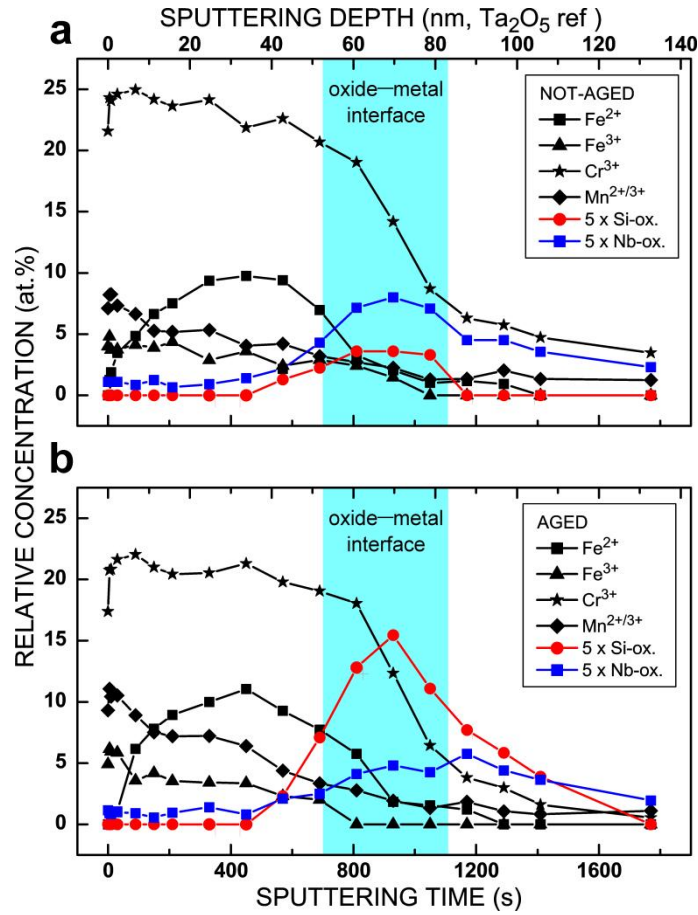
Fig. 4.6 – PES depth profiles showing the oxidized components of Fe, Cr, Mn, Si and Nb for (a) NOT-AGED and (b) AGED EN 1.4509 (Fe–19Cr–(Ti,Nb)) samples after 30 min oxidation in ambient air at 650 °C. [Paper IV]

Despite the similarities in the oxide layer compositions, two significant material aging-induced differences were observed. Firstly, the Si to Nb ratio at the oxide–metal interface of the AGED sample was significantly increased in comparison to that of the NOT-AGED sample. This was influenced by the Laves phase in the AGED sample that bound preferentially free Nb from the alloy solution. Secondly, the Mn to Cr ratio in the oxide layer was increased for the AGED sample. From the concurrent increase in the SiO_2 concentration at the oxide–metal interface, it was concluded that the diffusion of Mn through SiO_2 is faster in comparison to Cr. The formation of Mn-rich $(Mn,Cr)_3O_4$ spinel oxide on the top surface has beneficial effect against Cr volatilization in SOFC interconnect applications [12].

The electrical properties of the air-oxidized samples were analyzed by EIS at 25 °C. Fig. 4.7 shows the EIS data that was successfully interpreted by fitting with an equivalent electric circuit, depicted in Fig. 4.7(a) inset. The overall impedance was dominated by the transport

properties of the oxide layer due to its high electrical resistance R_{ox}. The most remarkable difference between the samples was the increase in the electrical resistance of the oxide scale from 0.74 MΩ cm^2 (NOT-AGED) to 4.6 MΩ cm^2 (AGED). Since the electrical resistivity of SiO$_2$ (1 × 10^{14} Ω cm) is significantly larger than the values for the other oxide compounds, e.g. Cr$_2$O$_3$ (1.3 × 10^3 Ω cm) [99], even small changes in the SiO$_2$ subscale reflected the value of R_{ox}. Therefore, the increased electrical resistance of the oxide scale formed on the AGED sample was attributed to the increased SiO$_2$ concentration at the oxide–metal interface.
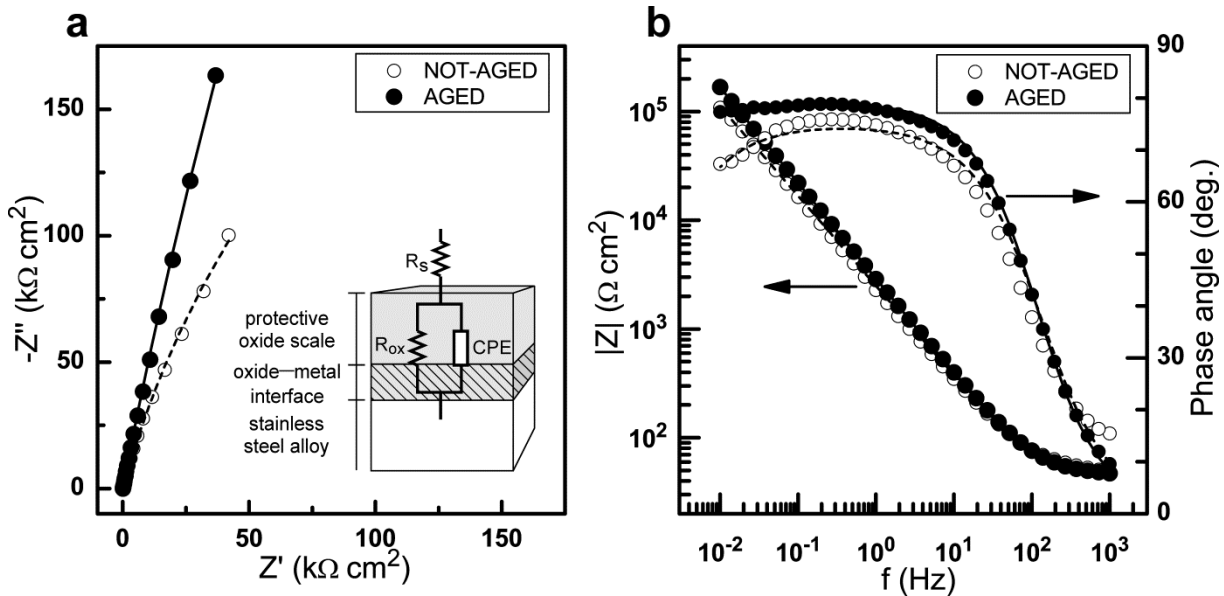

Fig. 4.7 – The EIS Nyquist plots (a) and the Bode plots (b) of the oxide scales on the NOT-AGED and the AGED EN 1.4509 (Fe–19Cr–(Ti,Nb)) samples followed by oxidation treatment in ambient air at 650 °C for 30 min. The inset shows schematic morphology of the oxide scale and the fitted equivalent circuit for the NOT-AGED (dashed line) and the AGED (solid line) samples. [Paper IV]

Then, surface segregation and oxidation experiments were conducted under a well-controlled UHV environment utilizing low-pressure O$_2$ exposures (i.e., low oxygen activity) at 650 °C. This approach allowed the direct observation of the interfacial compound formation by PES without the use of depth profiling. It was found that the surface enrichment of metallic Nb was strongly pronounced on the NOT-AGED sample after sputter cleaning and subsequent annealing at 650 °C (0 L) as shown in Fig. 4.8(a), whereas no thermally induced surface enrichment of Si^0 was observed at 650 °C (Fig. 4.8(b), 0 L). It should be noted that the surface concentration of Fe, Cr, Mn, and other alloying elements than Nb remained close to the bulk concentration on both samples. Interestingly, the binding energy value of the Nb 3d$_{5/2}$ peak corresponding to the Nb^0 on the FeCr alloy surface (203.0 eV) was shifted +0.7 eV in comparison to the pure Nb metal (202.3 eV) [104,105]. This binding energy shift was assigned to the formation of an FeNb intermetallic surface compound.
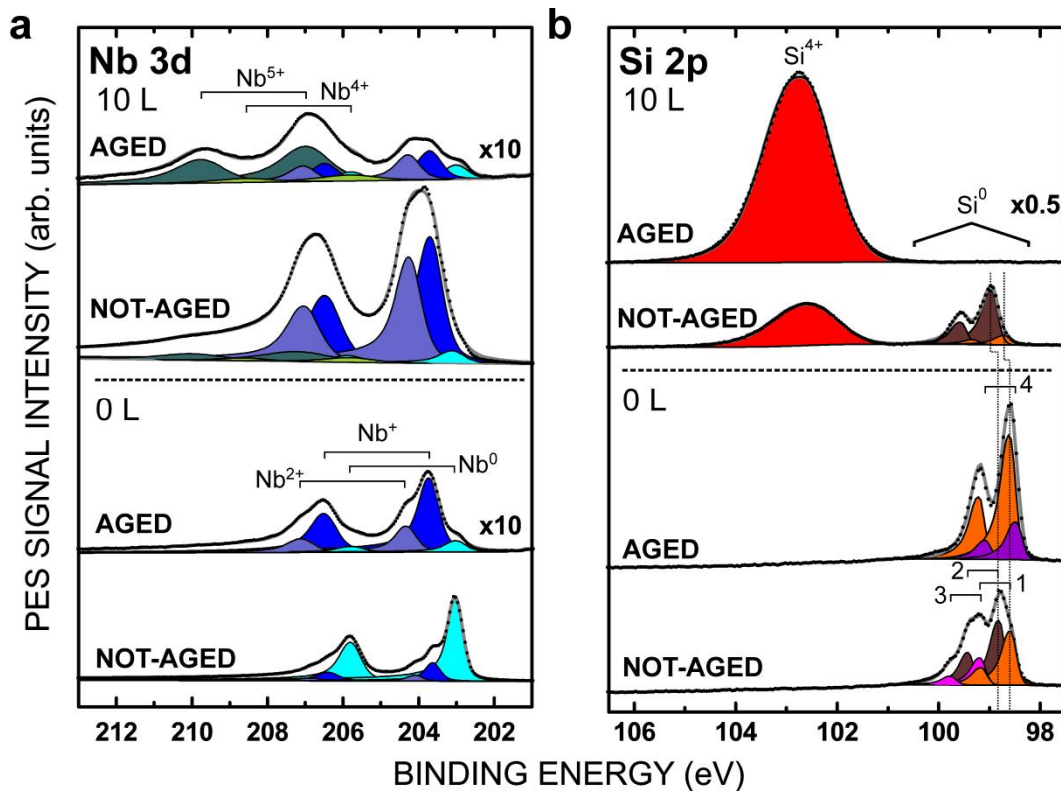
Fig. 4.8 – The PES high resolution spectra of (a) Nb 3d and (b) Si 2p transitions before and after 10 L oxygen exposure at 650 °C for the AGED and the NOT-AGED EN 1.4509 (Fe–19Cr–(Ti,Nb)) samples measured with hv = 400 eV. [Paper IV]

The surface enrichment of Nb had a remarkable influence on the initial surface oxidation of Si at 650 °C (Fig. 4.8(b), 10 L). The oxygen-induced surface segregation and oxidation of Si (SiO_2) was strongly hindered on the NOT-AGED sample that had initially a Nb-enriched surface. On the contrary, the SiO_2 formed more easily on the AGED sample, while oxidation of Nb proceeded to the highest oxidation state of 5+ (Nb_2O_5). The strong competition between Nb and Si for interfacial oxidation was further confirmed by a model system, in which a Nb overlayer (0.75 nm) was grown on the AGED sample utilizing a PVD technique [Paper IV]. The Nb overlayer had the same effect against the formation of electrically resistive Si oxides than the surface-enriched Nb on the NOT-AGED sample. Furthermore, the model system can be understood as an EN 1.4509 alloy with a slightly higher Nb alloying, which is expected to obtain enhanced electrical properties particularly in SOFC interconnect applications.

Fig. 4.9 shows the spatial distribution of SiO_2 on the AGED sample after the initial surface oxidation experiment. The formation of SiO_2 was clearly correlated with the location of the (FeNbSi)-type Laves phase particles on grain boundaries and on the grains (cf. Fig. 3.13). Therefore, the formation of the Laves phase in the bulk was concluded to result in the non-

uniform distribution of Si oxides at the oxide–metal interface of the EN 1.4509 alloy, which enhances the electrical properties of the alloy in comparison to the corresponding alloys with a uniform SiO_2 oxide subscale.
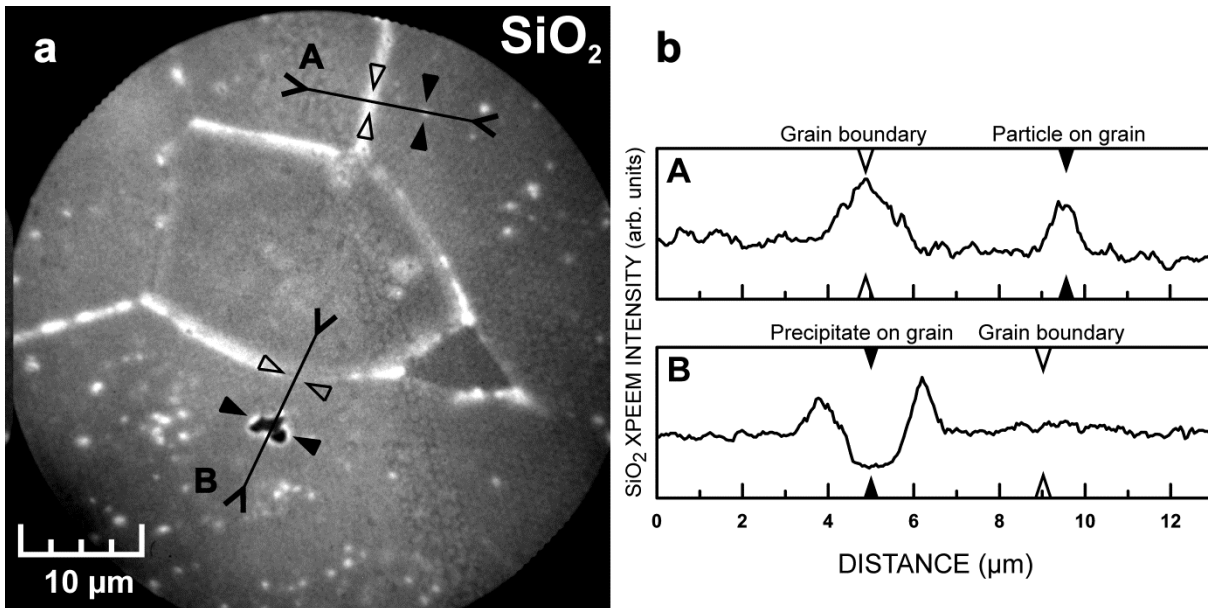

Fig. 4.9 – (a) An XPEEM image of the Si 2p (SiO_2) transition after 10 L oxygen exposure at 650 °C for the AGED EN 1.4509 (Fe–19Cr–(Ti,Nb)) sample, and (b) line profiles showing the intensity variation of the Si 2p signal across different microstructural features. A: A Laves-rich grain boundary and an intragranular Laves phase particle; B: A TiN-Nb(Fe)C precipitate and a Laves-poor grain boundary. [Paper III]

The influence of the Nb microalloying on the interfacial oxidation of EN 1.4509 at 650 °C is illustrated schematically in Fig. 4.10. Firstly, (a) Nb has a propensity for the formation of (FeNbSi)-type Laves intermetallic phase in the alloy upon prolonged aging at elevated temperatures. These Laves phase particles remove more effectively free Nb than Si from the alloy solution, which significantly hinders the surface segregation of Nb. Secondly, there is a strong competition between Nb and Si for interfacial oxidation at 650 °C: (b) the SiO_2 layer can form more easily on the aged alloy at the initial stages of oxidation, whereas the oxidation of Si is strongly limited by the surface enrichment and oxidation of Nb on the not-aged alloy surface. The same effect is observed at the oxide–metal interface after the oxidation in ambient air: (c) excess Nb in the not-aged sample efficiently hinders the formation of electrically resistive SiO_2 layer at the oxide–metal interface, which has direct consequences for the electrical resistivity of the oxide scale.
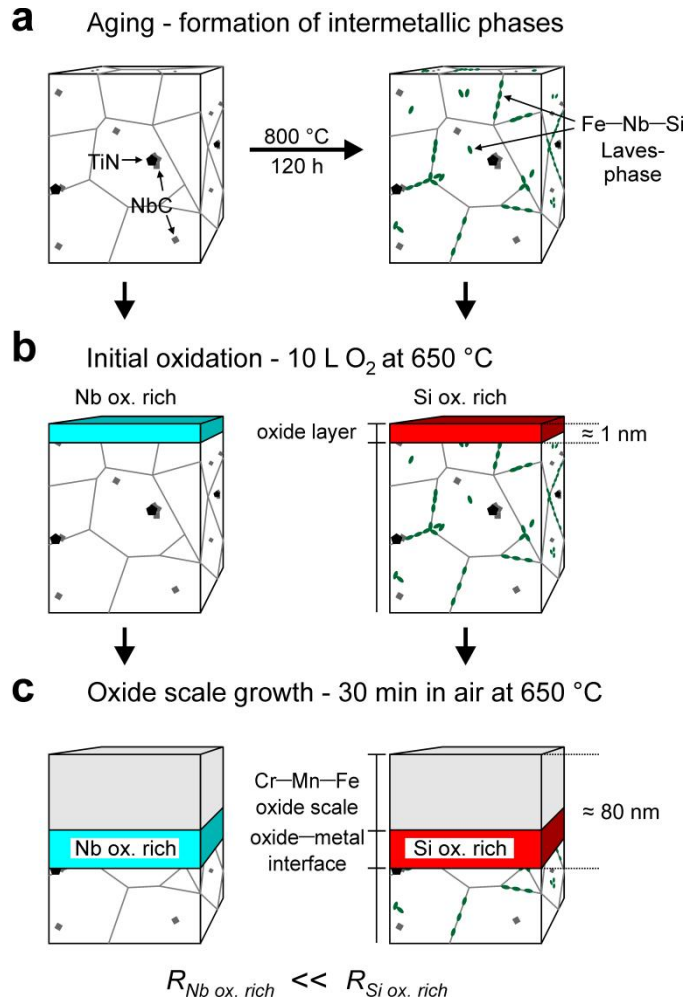
Fig. 4.10 – A schematic drawing of the interfacial oxidation of Nb and Si on the Laves-phase forming EN1.4509 (Fe–19Cr–(Ti,Nb)) stainless steel SOFC interconnect alloy at 650 °C: (a) the formation of intermetallic Fe–Nb–Si Laves phase upon aging at 800 °C; the composition and thickness of oxide layers after the initial oxidation in controlled ultra high vacuum environment (b) (low oxygen activity), and after the oxidation in ambient air (c) (high oxygen activity). *R* is electrical resistance. [Paper IV]

The beneficial role of excess Nb alloying for electrical properties of ferritic stainless steel alloys is attributed to its high segregation rate and the formation of conductive oxides at the interface. As a result, by the careful optimization of the Nb alloying, the formation of the electrically resistive SiO_2 at the oxide–metal interface can be controlled, which is of primary importance for the interconnect materials, such as EN 1.4509, in the SOFC applications, where the oxide scale must remain conductive.

5   SUMMARY AND OUTLOOK

Material corrosion has an enormous cost in the modern society. The loss of operation performance of a material due to corrosion is inevitable, but with an appropriate material choice it can be largely hindered or practically stopped. Mechanically strong stainless steel alloys are inherently corrosion-resistant materials, and therefore, widely applied as structural materials in demanding applications. Nevertheless, due to the new application areas together with more challenging operation conditions, the continuous development of stainless steel alloys and surface treatments is required.

Ferritic stainless steels are optimal materials for many energy applications, for example, energy conversion and exhaust systems. However, further alloy development is required concerning the high-temperature oxidation resistance due to the increased operation temperatures. Furthermore, new alloy materials that form an electrically conductive non-volatile oxide layer under high-temperature moist conditions are required for the solid-oxide fuel cell interconnect applications. On the other hand, the development of novel surface treatments that rely on reducing gas atmospheres (e.g., bright annealing) require parameter optimization in order to produce a nanoscale passive layer with the optimum composition and appearance. These material challenges are related to the formation and properties of the protective oxide layer on FeCr-alloy surfaces.

In order to overcome the current challenges, the oxidation phenomena need to be investigated starting from the segregation of alloying elements and the initial stages of oxidation. In this work, the oxidation phenomena of non-stabilized and Ti–Nb stabilized ferritic stainless steel alloys were investigated at 50–800 °C by PES and EIS. The versatile exploitation of the PES methods, including synchrotron radiation mediated PES, photoemission electron microscopy (PEEM), and inelastic electron energy-loss background analysis, provided new information concerning the influence of microalloying and adsorbate mediated segregation on the oxidation kinetics and mechanisms.

The oxidation resistance of an FeCr alloy is well known to increase with the increasing Cr bulk concentration. On the other hand, the surface concentration of Cr can be increased by controlled surface treatments without increasing the bulk concentration. The surface enrichment of Cr can be induced by H_2O preadsorption at low temperatures and by thermally induced cosegregation with N at high temperatures. At all temperatures, the Cr enriched

surface is beneficial against further oxidation by O_2, but the effect is the most pronounced at low temperatures where thermal diffusion of ions is not fast enough to support the oxidation.

Microalloying ferritic stainless steel with Ti and Nb effectively hinders the thermally induced cosegregation of Cr with N. At elevated temperatures, Ti and Nb segregate to the surface and affect the oxidation properties by forming stable oxides at the oxide–metal interface together with SiO_2 and other stable oxides. Particularly, Nb microalloying has significant influence on the oxidation properties at 650 °C. Firstly, there is a strong competition between Nb and Si for the interfacial oxidation: the excess Nb efficiently hinders the formation of electrically resistive SiO_2 layer at the oxide–metal interface. The beneficial role of Nb is attributed to its high segregation rate and the formation of conductive oxides at the interface. Secondly, the Nb alloying induces the formation of (FeNbSi)-type Laves intermetallic phase in the alloy, which results in the non-uniform distribution of SiO_2 at the interface. On the other hand, the Laves phase particles remove more effectively free Nb than Si from the alloy solution, and therefore, allow the SiO_2 layer to form more easily. However, the SiO_2-rich oxide–metal interface favors the formation of Mn-enriched $(Mn,Cr)_3O_4$ spinel oxide on the top surface, which is beneficial against Cr volatilization.

These new results concerning the surface segregation and oxidation of FeCr alloys can be applied to design ferritic stainless steel alloys and surface treatments that facilitate the formation of the protective oxide layer with the optimum composition under various demanding application conditions, particularly, in the SOFCs.

Future work is required to explore how to best increase the electrical conductivity of stainless steels in solid-oxide fuel cell applications. The microalloying with Nb was shown beneficial in this work, but its concentration was not yet optimized. In addition, microalloying with other elements, such as Mo, can be considered, but the second phase effects must be emphasized. On the other hand, the investigation of microalloying can be directed to improve other surface properties, for example, high-temperature oxidation resistance. The related phenomena are affected by the local defects (e.g., grain boundaries and precipitates), and therefore, the investigations with PEEM should be continued. Particularly, *in situ* PEEM studies of the valence band structure can provide further understanding of the conducting properties of the surface oxides. In contrast, the oxide layer volatilization and its prevention can be studied *in situ* by APPES under elevated pressure conditions.

REFERENCES

[1] 100 Years of Stainless Steel, The International Stainless Steel Forum (ISSF), http://www.stainlesssteelcentenary.info/, (accessed 30.11.2012).

[2] G.H. Koch, M.P.H. Brongers, N.G. Thompson, Y.P. Virmani, J.H. Payer, Corrosion Cost and Preventive Stratèges in the United States, Federal Highway Administration: Publication No. FHWA-RD-01-156. (2001).

[3] G.Y. Lai, High-Temperature Corrosion and Materials Applications, 1st ed., ASM International, USA, 2007.

[4] K.H. Lo, C.H. Shek, J.K.L. Lai, Recent developments in stainless steels, Mater. Sci. Eng., R. 65 (2009) 39–104.

[5] R.W.K. Honeycombe, H.K.D.H. Bhadeshia, Steels: Microstructure and Properties, 2nd ed., Edward Arnold, London, 1995.

[6] The Ferritic Solution, The International Stainless Steel Forum (ISSF), http://www.world stainless.org/Files/issf/non-image-files/PDF/ISSF_The_Ferritic_Solution_English.pdf, (accessed 30.11.2012).

[7] Recycling stainless steel, The International Stainless Steel Forum (ISSF), http://www.worldstainless.org/news/show/161, (accessed 30.11.2012).

[8] P.R. Rios, R.L. Plaut, A.F. Padilha, Stainless Steel Heat Treatment, in: G.E. Totten (Ed.), Steel Heat Treatment - Metallurgy and Technologies, CRC Press, 2006.

[9] J. Douthett, Heat Treating of Stainless Steels, in: D.L. Olsson et al. (Eds.), Heat Treating, ASM Handbook, Vol. 4, ASM International, 1991, pp. 769–792.

[10] J.F. Grubb, T. DeBold, J.D. Fritz, Corrosion of Wrought Stainless Steels, in: S.D. Cramer, B.S. Covino Jr. (Eds.), Corrosion: Materials, ASM Handbook, Vol. 13B, ASM International, 2005, pp. 54–77.

[11] G. Kienel, Degassing Processes (Converter Metallurgy), in: S. Viswanathan et al. (Eds.), Casting, ASM Handbook, Vol. 15, 1988, pp. 426–431.

[12] F. Jeffrey W., Synergism in the design of interconnect alloy–coating combinations for solid oxide fuel cells, Scr. Mater. 65 (2011) 73–77.

[13] D.J. Young, High Temperature Oxidation and Corrosion of Metals, Elsevier, Oxford, UK, 2008.

[14] J.R. Davis, Surface Engineering of Stainless Steels, in: C.M. Cotell, J.A. Sprague and F.A. Smidt (Eds.), Surface Engineering, ASM Handbook, Vol. 5, ASM International, 1994, pp. 741–761.

[15] G.A. Somorjai, Y. Li, Introduction to Surface Chemistry and Catalysis, 2nd ed., John Wiley & Sons, Inc., Hoboken, New Jersey, 2010.

[16] H.J. Grabke, V. Leroy, H. Viefhaus, Segregation on the Surface of Steels in Heat Treatment and Oxidation, ISIJ Int. 35 (1995) 95–113.

[17] H.J. Grabke, Segregation and oxidation, Mater. Tehnol. 40 (2006) 39–47.

[18] E. Park, B. Hüning, M. Spiegel, Evolution of near-surface concentration profiles of Cr during annealing of Fe–15Cr polycrystalline alloy, Appl. Surf. Sci. 249 (2005) 127–138.

[19] C. Uebing, Two-dimensional transition metal compounds with carbon, nitrogen and oxygen on BCC(100) metal and alloy surfaces, Prog. Solid State Chem. 26 (1998) 155–240.

[20] L. Vitos, A.V. Ruban, H.L. Skriver, J. Kollár, The surface energy of metals, Surf. Sci. 411 (1998) 186–202.

[21] M. Ropo, K. Kokko, M.P.J. Punkkinen, S. Hogmark, J. Kollár, B. Johansson, L. Vitos, Theoretical evidence of the compositional threshold behavior of FeCr surfaces, Phys. Rev. B. 76 (2007) 220401.

[22] M. Ropo, K. Kokko, E. Airiskallio, M.P.J. Punkkinen, S. Hogmark, J. Kollár, B. Johansson, L. Vitos, First-principles atomistic study of surfaces of Fe-rich Fe-Cr, J. Phys.: Condens. Matter. 23 (2011) 265004.

[23] M. Polak, L. Rubinovich, Alloy surface segregation and ordering phenomena: recent progress, in: D.P. Woodruff (Ed.), The Chemical Physics of Solid Surfaces, Vol. 10, Surface Alloys and Alloy Surfaces, Elsevier, Amsterdam, 2002, pp. 86–117.

[24] E. McCafferty, Introduction to Corrosion Science, Springer, 2010.

[25] W.M. Haynes, D.R. Lide, CRC Handbook of Chemistry and Physics, 2011.

[26] M.W. Chase, C.A. Davies, J.R. Downey, D.J. Frurip, R.A. McDonald, A.N. Syverud, NIST JANAF Thermochemical Tables, 2012 (1985).

[27] M.W. Coughlin, Contributions to the Data on Theoretical Metallurgy, US Government Printing Office, Washington, DC, 1954.

[28] J. Oudar, Introduction to Surface Reactions: Adsorption from Gas Phase, in: P. Marcus (Ed.), Corrosion Mechanisms in Theory and Practice, 2nd ed., Marcel Dekker Inc., New York, 2002, pp. 19–51.

[29] F.P. Fehlner, M.J. Graham, Thin Oxide Film Formation on Metals, in: P. Marcus (Ed.), Corrosion Mechanisms in Theory and Practice, 2nd ed., Marcel Dekker Inc., New York, 2002, pp. 171–187.

[30] V. Maurice, P. Marcus, Passive films at the nanoscale, Electrochim. Acta 84 (2012) 129–138.

[31] P. Marcus, Surface science approach of corrosion phenomena, Electrochim. Acta. 43 (1998) 109–118.

[32] F.H. Stott, G.C. Wood, J. Stringer, The influence of alloying elements on the development and maintenance of protective scales, Oxid. Met. 44 (1995) 113–145.

[33] J. Robertson, M.I. Manning, Healing layer formation in Fe–Cr–Si ferritic steels, Mater. Sci. Technol. 5 (1989) 741–753.

[34] S.R.J. Saunders, M. Monteiro, F. Rizzo, The oxidation behaviour of metals and alloys at high temperatures in atmospheres containing water vapour: A review, Prog. Mater Sci. 53 (2008) 775–837.

[35] R.J.F. Gerwen, Systems and Applications, in: S.C. Singhal and K. Kendall (Eds.), High-Temperature Solid Oxide Fuel Cells: Fundamentals, Design and Applications, 1st ed., Elsevier, UK, 2003, pp. 363–392.

[36] Y. Inoue, M. Kikuchi, Present and Future Trends of Stainless Steel for Automotive Exhaust System, Nippon Steel Technical Report. (2003) 62–69.

[37] J. Douthett, Automotive Exhaust System Corrosion, in: S.D. Cramer, B.S. Covino Jr. (Eds.), Corrosion: Environments and Industries, ASM Handbook, Vol 13C, 2006, pp. 519–530.

[38] B.C.H. Steele, A. Heinzel, Materials for fuel-cell technologies, Nature. 414 (2001) 345–352.

[39] Z. Yang, Recent advances in metallic interconnects for solid oxide fuel cells, Int. Mater. Rev. 53 (2008) 39–54.

[40] E.D. Wachsman, K.T. Lee, Lowering the Temperature of Solid Oxide Fuel Cells, Science. 334 (2011) 935–939.

[41] N. Shaigan, W. Qu, D.G. Ivey, W. Chen, A review of recent progress in coatings, surface modifications and alloy developments for solid oxide fuel cell ferritic stainless steel interconnects, J. Power Sources. 195 (2010) 1529–1542.

[42] J. Fergus, Z. Yang, Interconnects, in: J. Fergus et al. (Ed.): Solid Oxide Fuel Cells: materials properties and performance, CRC Press, 2008, pp. 179–212.

[43] J.-H. Wang, M. Liu, Z. Cheng, Anodes, in: J. Fergus et al. (Ed.): Solid Oxide Fuel Cells: materials properties and performance, CRC Press, 2008, pp. 73–129.

[44] R.A. Antunes, M.C.L. Oliveira, G. Ett, V. Ett, Corrosion of metal bipolar plates for PEM fuel cells: A review, Int. J. Hydrogen Energy. 35 (2010) 3632–3647.

[45] M. Aindow, S.P. Alpay, Y. Liu, J.V. Mantese, B.S. Senturk, Base metal alloys with self-healing native conductive oxides for electrical contact materials, Appl. Phys. Lett. 97 (2010) 152103.

[46] Z. Zeng, K. Natesan, Z. Cai, S.B. Darling, The role of metal nanoparticles and nanonetworks in alloy degradation, Nat. Mater. 7 (2008) 641–646.

[47] K. Lahtonen, M. Lampimaki, P. Jussila, M. Hirsimaki, M. Valden, Instrumentation and analytical methods of an x-ray photoelectron spectroscopy - scanning tunneling microscopy surface analysis system for studying nanostructured materials, Rev. Sci. Instrum. 77 (2006) 083901.

[48] R. Nyholm, J.N. Andersen, U. Johansson, B.N. Jensen, I. Lindau, Beamline I311 at MAX-LAB: a VUV/soft X-ray undulator beamline for high resolution electron spectroscopy, Nucl. Instrum. Methods Phys. Res. , Sect. A. 467–468 (2001) 520–524.

[49] See www.elmitec.de for details of the SPELEEM III instrument manufactured by Elmitec GmbH.

[50] A.V. Naumkin, A. Kraut-Vass, C.J. Powell, NIST XPS Database 20, Version 4.0 (Web Version). National Institute of Standards and Technology 2008, http://srdata.nist.gov/xps/.

[51] B.D. Ratner, D.G. Castner, Electron Spectroscopy for Chemical Analysis, in: J.C. Vickerman (Ed.), Surface Analysis - the Principal Techniques, John Wiley & Sons Ltd., Chichester, 1997, pp. 43–98.

[51] N.S. McIntyre, X-ray photoelectron spectroscopic studies of iron oxides, Anal. Chem. 49 (1977) 1521–1529.

[53] K.W. Kolasinski, Surface Science: Foundations of Catalysis and Nanoscience, 2nd ed., John Wiley & Sons Ltd., Chichester, 2008.

[54] D. Briggs, XPS: Basic Principles, Spectral Features and Qualitative Analysis, in: D. Briggs and J.T. Grant (Eds.), Surface Analysis by Auger and X-Ray Photoelectron Spectroscopy, IM Publications, Trowbridge, 2003, pp. 31–56.

[55] M.P. Seah, W.A. Dench, Quantitative electron spectroscopy of surfaces: A standard data base for electron inelastic mean free paths in solids, Surf. Interface Anal. 1 (1979) 2–11.

[56] J.J. Yeh, I. Lindau, Atomic subshell photoionization cross sections and asymmetry parameters: $1 \leq Z \leq 103$, Atomic Data and Nuclear Data Tables. 32 (1985) 1–155.

[57] G. Margaritondo, X-ray Photoelectron Spectroscopy and Imaging at Synchrotrons, in: D. Briggs and J.T. Grant (Eds.), Surface Analysis by Auger and X-Ray Photoelectron Spectroscopy, IM Publications, Trowbridge, 2003, pp. 733–748.

[58] S. Kaya, H. Ogasawara, L. Näslund, J. Forsell, H.S. Casalongue, D.J. Miller, A. Nilsson, Ambient-pressure photoelectron spectroscopy for heterogeneous catalysis and electrochemistry, Catalysis Today (2012), http://dx.doi.org/10.1016/j.cattod.2012.08.005.

[59] M. Salmeron, R. Schlögl, Ambient pressure photoelectron spectroscopy: A new tool for surface science and nanotechnology, Surf. Sci. Rep. 63 (2008) 169–199.

[60] S. Yamamoto, T. Kendelewicz, J.T. Newberg, G. Ketteler, D.E. Starr, E.R. Mysak, K.J. Andersson, H. Ogasawara, H. Bluhm, M. Salmeron, G.E. Brown Jr., A. Nilsson, Water adsorption on α-Fe$_2$O$_3$ (0001) at near ambient conditions, J. Phys. Chem. C. 114 (2010) 2256–2266.

[61] C. Zhang, M.E. Grass, A.H. McDaniel, S.C. DeCaluwe, F.E. Gabaly, Z. Liu, K.F. McCarty, R.L. Farrow, M.A. Linne, Z. Hussain, G.S. Jackson, H. Bluhm, B.W. Eichhorn, Measuring fundamental properties in operating solid oxide electrochemical cells by using in situ X-ray photoelectron spectroscopy, Nat. Mater. 9 (2010) 944–949.

[62] A. Nilsson, Applications of core level spectroscopy to adsorbates, J. Electron Spectrosc. Relat. Phenom. 126 (2002) 3–42.

[63] P. Wernet, D. Nordlund, U. Bergmann, M. Cavalleri, N. Odelius, H. Ogasawara, L.Å. Näslund, T.K. Hirsch, L. Ojamäe, P. Glatzel, L.G.M. Pettersson, A. Nilsson, The Structure of the First Coordination Shell in Liquid Water, Science. 304 (2004) 995–999.

[64] J.G. Chen, NEXAFS investigations of transition metal oxides, nitrides, carbides, sulfides and other interstitial compounds, Surf. Sci. Rep. 30 (1997) 1–152.

[65] S. Granroth, W. Olovsson, E. Holmström, R. Knut, M. Gorgoi, S. Svensson, O. Karis, Understanding interface properties from high kinetic energy photoelectron spectroscopy and first principles theory, J. Electron Spectrosc. Relat. Phenom. 183 (2011) 80–93.

[66] K. Andersson, M. Nyberg, H. Ogasawara, D. Nordlund, T. Kendelewicz, C.S. Doyle, G.E. Brown, L.G.M. Pettersson, A. Nilsson, Experimental and theoretical characterization of the structure of defects at the pyrite FeS$_2$(100) surface, Phys. Rev. B. 70 (2004) 1–5.

[67] B.P. Payne, M.C. Biesinger, N.S. McIntyre, X-ray photoelectron spectroscopy studies of reactions on chromium metal and chromium oxide surfaces, J. Electron Spectrosc. Relat. Phenom. 184 (2011) 29–37.

[68] A.P. Grosvenor, B.A. Kobe, M.C. Biesinger, N.S. McIntyre, Investigation of multiplet splitting of Fe 2p XPS spectra and bonding in iron compounds, Surf. Interface Anal. 36 (2004) 1564–1574.

[69] J.F. Moulder, W.F. Stickle, P.E. Sobol, K.D. Bomben, Handbook of X-Ray Photoelectron Spectroscopy, Perkin-Elmer Corporation, 1992.

[70] L. Kövér, Chemical Effects in XPS, in: D. Briggs and J.T. Grant (Eds.), Surface Analysis by Auger and X-Ray Photoelectron Spectroscopy, IM Publications, Trowbridge, 2003, pp. 421–464.

[71] N. Fairley, XPS Lineshapes and Curve Fitting, in: D. Briggs and J.T. Grant (Eds.), Surface Analysis by Auger and X-Ray Photoelectron Spectroscopy, IM Publications, Trowbridge, 2003, pp. 397–420.

[72] V.S. Smentkowski, Trends in sputtering, Prog. Surf. Sci. 64 (2000) 1–58.

[73] N. Alov, D. Kutsko, Ion-beam reduction of the surface of higher niobium oxide, J. Surf. Investig-X-ray Synchro. 4 (2010) 232–235.

[74] Operation of the Angle Resolving Lens on Theta Probe, Application Note: 31003, Thermo Scientific, http://www.thermoscientific.com, (accessed 30.11.2012).

[75] P. Strasser, S. Koh, T. Anniyev, J. Greeley, K. More, C. Yu, Z. Liu, S. Kaya, D. Nordlund, H. Ogasawara, M.F. Toney, A. Nilsson, Lattice-strain control of the activity in dealloyed core-shell fuel cell catalysts, Nat. Chem. 2 (2010) 454–460.

[76] W. Fredriksson, S. Malmgren, T. Gustafsson, M. Gorgoi, K. Edström, Full depth profile of passive films on 316L stainless steel based on high resolution HAXPES in combination with ARXPS, Appl. Surf. Sci. 258 (2012) 5790–5797.

[77] A.P. Grosvenor, B.A. Kobe, N.S. McIntyre, Studies of the oxidation of iron by water vapour using X-ray photoelectron spectroscopy and QUASES™, Surf. Sci. 572 (2004) 217–227.

[78] S. Tougaard, QUASES: Software for Quantitative XPS/AES of Surface Nano-structures by Analysis of the Peak Shape and Background, Version 5.0 (2003).

[79] S. Tougaard, Quantification of Nano-structures by Electron Spectroscopy, in: D. Briggs and J.T. Grant (Eds.), Surface Analysis by Auger and X-Ray Photoelectron Spectroscopy, IM Publications, Trowbridge, 2003, pp. 295–343.

[80] S. Tougaard, Accuracy of the non-destructive surface nanostructure quantification technique based on analysis of the XPS or AES peak shape, Surf. Interface Anal. 26 (1998) 249–269.

[81] M. Lampimäki, K. Lahtonen, P. Jussila, M. Hirsimäki, M. Valden, Morphology and composition of nanoscale surface oxides on Fe–20Cr–18Ni{1 1 1} austenitic stainless steel, J. Electron Spectrosc. Relat. Phenom. 154 (2007) 69–78.

[82] S. Tanuma, C.J. Powell, D.R. Penn, Calculations of electron inelastic mean free paths. V. Data for 14 organic compounds over the 50-2000 eV range, Surf. Interface Anal. 21 (1994) 165–176.

[83] G. Margaritondo, Photoelectron spectromicroscopy and spectronanoscopy at synchrotrons: Growing impact on life sciences and materials science, J. Electron Spectrosc. Relat. Phenom. 178–179 (2010) 273–291.

[84] A. Barinov, P. Dudin, L. Gregoratti, A. Locatelli, T. Onur Menteş, M. Ángel Niño, M. Kiskinova, Synchrotron-based photoelectron microscopy, Nucl. Instrum.Methods Phys. Res. Sect. A. 601 (2009) 195–202.

[85] O. Renault, M. Lavayssière, A. Bailly, D. Mariolle, N. Barrett, Core level photoelectron spectromicroscopy with Al $K_{\alpha1}$ excitation at 500 nm spatial resolution, J. Electron Spectrosc. Relat. Phenom. 171 (2009) 68–71.

[86] E. Bauer, A brief history of PEEM, J. Electron Spectrosc. Relat. Phenom. 185 (2012) 314–322.

[87] D.D. Macdonald, Reflections on the history of electrochemical impedance spectroscopy, Electrochim. Acta. 51 (2006) 1376–1388.

[88] F. Mansfeld, Electrochemical Methods of Corrosion Testing, in: S.D. Cramer, B.S. Covino Jr. (Eds.), Corrosion: Fundamentals, Testing, and Protection, ASM Handbook, Vol 13A, ASM International, 2003, pp. 446–462.

[89] D.D. Macdonald, The history of the Point Defect Model for the passive state: A brief review of film growth aspects, Electrochim. Acta. 56 (2011) 1761–1772.

[90] E. Barsoukov, J.R. Macdonald, Impedance spectroscopy theory, experiments and applications, 2nd ed., John Wiley & Sons, Inc., Hoboken, New Jersey, 2005.

[91] D.D. Macdonald, E. Sikora, G. Engelhardt, Characterizing electrochemical systems in the frequency domain, Electrochim. Acta. 43 (1998) 87–107.

[92] X. Cheng, Z. Feng, C. Li, C. Dong, X. Li, Investigation of oxide film formation on 316L stainless steel in high-temperature aqueous environments, Electrochim. Acta. 56 (2011) 5860–5865.

[93] J. Wielant, V. Goossens, R. Hausbrand, H. Terryn, Electronic properties of thermally formed thin iron oxide films, Electrochim. Acta. 52 (2007) 7617–7625.

[94] H. Sun, X. Wu, E. Han, Effects of temperature on the oxide film properties of 304 stainless steel in high temperature lithium borate buffer solution, Corros. Sci. 51 (2009) 2840–2847.

[95] J.R. Lince, S.V. Didziulis, D.K. Shuh, T.D. Durbin, J.A. Yarmoff, Interaction of O_2 with the $Fe_{0.84}Cr_{0.16}$(001) surface studied by photoelectron spectroscopy, Surf. Sci. 277 (1992) 43–63.

[96] D.A. Harrington, A. Wieckowski, S.D. Rosasco, B.C. Schardt, G.N. Salaita, A.T. Hubbard, J.B. Lumsden, Films formed on well-defined stainless steel single-crystal surfaces in oxygen and water: studies of the (111) plane by LEED, Auger and XPS, Corros. Sci. 25 (1985) 849–869.

[97] P. Jussila, H. Ali-Löytty, K. Lahtonen, M. Hirsimäki, M. Valden, Effect of surface hydroxyl concentration on the bonding and morphology of aminopropylsilane thin films on austenitic stainless steel, Surf. Interface Anal. 42 (2010) 157–164.

[98] M. Honkanen, M. Hoikkanen, M. Vippola, J. Vuorinen, T. Lepistö, P. Jussila, H. Ali-Löytty, M. Lampimäki, M. Valden, Characterization of silane layers on modified stainless steel surfaces and related stainless steel–plastic hybrids, Appl. Surf. Sci. 257 (2011) 9335–9346.

[99] W.Z. Zhu, S.C. Deevi, Development of interconnect materials for solid oxide fuel cells, Mater. Sci. Eng., A. 348 (2003) 227–243.

[100] R.J. Cava, B. Batlogg, J.J. Krajewski, H.F. Poulsen, P. Gammel, W.F. Peck, L.W. Rupp, Electrical and magnetic properties of $Nb_2O_{5-\delta}$ crystallographic shear structures, Phys. Rev. B. 44 (1991) 6973–6981.

[101] J. Froitzheim, G.H. Meier, L. Niewolak, P.J. Ennis, H. Hattendorf, L. Singheiser, W.J. Quadakkers, Development of high strength ferritic steel for interconnect application in SOFCs, J. Power Sources. 178 (2008) 163–173.

[102] T.J. Juuti, L.P. Karjalainen, E.P. Heikkinen, Precipitation of Si and its Influence on Mechanical Properties of Type 441 Stainless Steel, Adv. Mater. Res. 409 (2011) 690–695.

[103] B. Hua, Y. Kong, W. Zhang, J. Pu, B. Chi, L. Jian, The effect of Mn on the oxidation behavior and electrical conductivity of Fe–17Cr alloys in solid oxide fuel cell cathode atmosphere, J. Power Sources. 196 (2011) 7627–7638.

[104] Q. Ma, P. Ryan, J.W. Freeland, R.A. Rosenberg, Thermal effect on the oxides on Nb(100) studied by synchrotron-radiation x-ray photoelectron spectroscopy, J. Appl. Phys. 96 (2004) 7675–7680.

[105] H. Habazaki, M. Yamasaki, T. Ogasawara, K. Fushimi, H. Konno, K. Shimizu, T. Izumi, R. Matsuoka, P. Skeldon, G.E. Thompson, Thermal degradation of anodic niobia on niobium and oxygen-containing niobium, Thin Solid Films. 516 (2008) 991–998.